(4)

PENNSTATE

DTIC FILE COPY

AD-A213 874

Applied Research Laboratory

MODIFICATIONS OF THE PENN STATE BOUNDARY LAYER RESEARCH FACILITY FOR BOUNDARY LAYER/STRUCTURE INTERACTION EXPERIMENTAL RESEARCH

C. B. Burroughs

Technical Memorandum
File No. TM 89-38
23 August 1989

Copy No. 5

CS

DISTRIBUTION UNLIMITED

Department of the Navy
Space and Naval Warfare Systems Command

Contract No. N00039-88-C-0051

P.O. Box 30
State College, PA 16804
(814) 865-3031

PENNSTATE

Applied Research Laboratory

MODIFICATIONS OF THE PENN STATE BOUNDARY LAYER RESEARCH FACILITY FOR BOUNDARY LAYER/STRUCTURE INTERACTION EXPERIMENTAL RESEARCH

C. B. Burroughs

Technical Memorandum
File No. TM 89-38
23 August 1989

DISTRIBUTION UNLIMITED

Issued as IM on 15 June 1989

P.O. Box 30
State College, PA 16804
(814) 865-3031

From: C. B. Burroughs

Subject: Modifications of the Penn State Boundary Layer Research Facility for Boundary Layer/Structure Interaction Experimental Research

References: See page 18

Abstract: Modifications to the Penn State Boundary Layer Research Facility (BLRF) have been made so that low wavenumber turbulent boundary layer (TBL) wall pressure fluctuation spectra can be measured. In addition, fundamental experimental research on boundary layer/structure interaction can be conducted. Modifications include the design and fabrication of a new test section to accommodate a long flat elastic test plate in contact with the boundary layer and extensive treatments to reduce background vibration levels in the test plate. The design, fabrication and installation of these modifications are described.

From: C. B. Burroughs

References: See Page 18

Subject: Modifications of the Penn State Boundary Layer Research Facility for Boundary Layer/Structure Interaction Experimental Research

Abstract: Modifications to the Penn State Boundary Layer Research Facility (BLRF) have been made so that low wavenumber turbulent boundary layer (TBL) wall pressure fluctuation spectra can be measured, as well as fundamental experimental research on boundary layer/structure interaction conducted. Modifications include the design and fabrication of a new test section to accommodate a long flat elastic test plate in contact with the boundary layer and extensive treatments to reduce background vibration levels in the test plate. The design, fabrication and installation of these modifications are described.

Table of Contents

List of Tables

List of Figures

List of Figures (Cont.)

1.0 Introduction

The excitation of structures by turbulent boundary layer (TBL) wall pressure fluctuations depends on the wavenumber frequency coupling between the wall pressures and the admittance of the underlying structure. Because the admittance of structures is high at low wavenumbers where free bending wave propagation and resonances occur in the structure, the TBL wall pressures at low wavenumbers play an important role in the response of TBL-excited structures. However, TBL spectral levels at low wavenumbers have been difficult to measure primarily because of the unavailability of wavenumber filters strong enough to reject the high TBL spectra around the convective wavenumber so that the TBL spectra at low wavenumbers can be accurately measured.

Attempts have been made to measure the low wavenumber TBL spectra with arrays of flush-mounted pressure sensors [1,2,3] and with membranes [4] and plates [5]. However, these measurements have failed to produce consistent results. The inconsistency in measurement results may be attributed to contamination of the results by background noise in the measurement facilities or by high wavenumber TBL spectra that enter the wavenumber filter beam pattern at wavenumbers outside the main lobe.

Improvements in the wavenumber filter to increase the rejection of TBL spectra at higher wavenumbers in the convective ridge in the TBL spectra can be obtained by localizing the TBL downstream on a long flat plate and measuring the response of the plate upstream under laminar flow. With this approach, the wavenumber filtering consists of three parts; 1) response of the downstream portion of the plate under the localized TBL, 2) propagation of the TBL-excited vibrations in the plate from downstream to the measurement location on the plate upstream under laminar flow and 3) vibration measurement with a line array of accelerometers on the upstream portion of the plate. The first filtering action is provided by the admittance of the plate which is high at the free-bending wavenumber in the plate and decreases for increasing wavenumbers. This is the wavenumber filtering used by Martin, and Leehey [4] and Jameson [5]. In the propagation of the TBL-excited vibrations from the downstream end directly under the localized TBL to the measurement location upstream, only free vibrations will propagate. Since free propagation in the plate will occur only at the free bending wavenumbers, vibrations at other than free bending wavenumbers will be attenuated exponentially during propagation from the downstream TBL-excitation locations in the plate to the upstream measurement location. The third filtering action is provided by steering the line array of measurement accelerometers on the plate to the measurement low wavenumber equal to the free bending wavenumber of the plate. This filtering action is similar to that used by Blake and Chase [1] and Geib and Farabee [2,3] with arrays of flush-mounted pressure sensors.

The facility requirements for the measurement procedure outlined above are: 1) a long elastic structure subject to TBL excitation, 2) laminar flow at the upstream end of the elastic structure and 3) background vibration levels in the structure that are lower than the levels of the vibration induced in the structure by the TBL. To satisfy these requirements,

modifications to the ARL Penn State Boundary Layer Research Facility (BLRF) were made to install a long flat test plate in the test section and reduce background vibration levels in the test plate to levels below the levels of the vibrations generated by the TBL. Descriptions of these modifications and design considerations behind the modifications to the BLRF for low wavenumber TBL unsteady wall pressure spectral measurements are presented and discussed in this report. In Section 2.0, the design of the new test section to accommodate a long flat plate and the transition and diffuser sections required for the new test section are discussed. Reductions in the background vibration levels required in the BLRF for low wavenumber TBL spectral measurements and treatments for reducing the BLRF background vibration levels to the required levels are presented in Section 3.0. Section 4.0 contains a summary.

Although the modifications to the BLRF were motivated by the need to measure the low wavenumber TBL spectra, the modified BLRF has a much broader use. The modified BLRF will possess the following properties:

1) A thick boundary layer which facilitates detailed measurements of the flow inside the layer,

2) Low background vibration levels which reduce contamination of TBL-induced structural response measurements by background noise,

3) An elastic structure in contact with shear boundary layers for fluid/structure interaction,

4) The ability to generate and maintain laminar, transition or turbulent boundary layers, and

5) Measurement accessibility to the shear boundary layer

All of these properties are required for fundamental research on the interaction that occurs between fluid shear boundary layers and the vibration response of underlying elastic structures. The first and fourth of the properties listed above are present in the existing BLRF because the working medium in the BLRF is glycerine. The high viscosity of glycerine results in a thick boundary layer and Reynolds numbers that are low enough for laminar flow but high enough to maintain tripped turbulence. The second and third of the properties listed above are required to meet the original objective of measuring the low wavenumber TBL spectra. The fifth property was easily added during the modifications to the BLRF required to make low wavenumber TBL spectral measurements.

2.0 Test Section

2.1 Test Plate

Because the present BLRF test section has a circular cross-section, using a cylindrical test plate that would conform to the shape of the current test section would avoid the need to fabricate sections for transition from the current circular cross-section to a cross-section which would accommodate a

flat test plate. However, the curvature of a cylindrical plate will couple transverse displacements with in-plane displacements. The impedances for in-place displacements are much higher than the impedances for transverse displacements so that the drive impedance of a cylindrical plate will probably be higher than the drive impedance of a flat plate where, for displacements small relative to the plate thickness, the transverse displacements do not couple to in-plane displacements. Because TBL wall pressures couple primarily to transverse displacements of the underlying structure, a cylindrical plate would have a lower sensitivity as a transducer for the measurement of low wavenumber TBL wall pressures than a flat plate. To determine the sensitivity of a cylindrical plate to TBL excitation relative to the sensitivity of a flat plate, the impedances of cylindrical and flat plates to wavenumber drives are estimated and compared at frequencies of interest.

As outlined in Appendix A, cylindrical shell theory is used to estimate wavenumber impedances for both cylindrical and flat plates. As discussed in Appendix A, the flat plate is modeled as part of a cylindrical shell with a large radius so that the same boundary conditions for the cylindrical and flat plate can be used. The assumptions employed in applying cylindrical shell theory in Appendix A to model the wavenumber impedance of flat and cylindrical plates are:

1) The plates are long enough in the streamwise direction that the upstream and downstream ends can be ignored and the plate modeled as infinite in the streamwise direction.

2) The wavenumber drive is oriented in the streamwise direction with a finite width in the cross-stream direction.

3) The thickness of the plate is small compared to the radius of curvature of the plate.

4) The edges in the streamwise directions are simply supported so that the transverse displacement is zero and the moment and in-plane stress vanish at the edge.

For steel plates that are 1/8 inch thick and 6 inches wide, estimates of the wavenumber drive impedances were made as a function of drive wavenumber using the solutions given in Appendix A. The wavenumber drive was located 1 inch from the center of both the cylindrical and flat plates. For the cylindrical plate, a radius of 5.6 inches was used. This is the radius of the current BLRF test section. For the flat plate, a radius of curvature of 10 feet was used. At a frequency of 100 Hz, the estimated impedances for the cylindrical plate are higher than the impedances for the flat plate by about 10 dB as shown in Figure 1. Also, the number of peaks in impedance are higher for the cylindrical plate than for the flat plate.

Because the wavenumber impedance of a cylindrical plate, shaped to conform to the current BLRF test section, is higher than the impedance of a flat plate, the flat plate will have a higher sensitivity as a transducer for TBL spectral measurements than the cylindrical plate. Also, the flat plate

should have a smoother response to TBL excitation than the cylindrical plate. Therefore, a flat plate was selected for use in the BLRF as the transducer for low wavenumber TBL spectral measurements. To accommodate the flat plate in the BLRF test section, transition from the current circular cross-section to a cross-section with a flat portion for the test plate is included in the design of the BLRF modifications.

2.2 Transition and Diffuser Sections

Transition from the current circular cross-section to the cross-section of the test section with the flat plate will be made by a transition section. Downstream of the test section, the cross-section of the test section will be returned to the circular cross-section in the BLRF by a diffuser section. The transition and diffuser sections thereby provide the coupling between the new test section and the remainder of the existing BLRF. One of the requirements for the low wavenumber TBL spectral measurements is that the flow at the entrance to the new test section be laminar. Therefore, transition must be made without disturbing the laminar flow that currently exists at the exit from the settling section which will be the entrance to the transition section. The longer the transition section, the more gradual the transition and more likely laminar flow can be maintained. However, increasing the length increases fabrication costs. As a compromise between these two conflicting criteria, a length of three feet for the transition section was selected for investigation.

2.2.1 Flow Visualization Inside Model of Transition Section

A model of a transition section was fabricated from sheet metal for flow visualization measurements. The entrance was circular with a radius of 6 inches to match the radius of the exit from the ARL Penn State open jet facility. The air flow at the exit of the open jet facility (entrance to the model of the transition section) was laminar. The cross-section of the exit of the model transition section was comprised of two semi-circles separated by straight lines designed to model the cross-section of the new BLRF test section. As shown in Figure 2, the radii of the semi-circles is 4 1/2 inches. The two semi-circles are separated by 7 inches. These dimensions were selected to approximate those of the test section (See Section 2.3). The transition from circular entrance to the semi-circle flat plate exit was made by straight lines separating the semi-circles from the flat plates as shown in Figure 2. This design is simple to enhance ease of fabrication. The final design of the transition section, discussed later in this section, is an improvement over this simple design. For example, discontinuities in the derivatives of the surface profiles in the model are eliminated in the final design of the transition section. Therefore, the favorable results obtained on the model transition section indicate that favorable results should be obtained with the final transition section.

Using the procedure described in Appendix B, the flow was visualized with the smoke wire in the three positions shown in Figure 3. At each of these positions, flow visualizations were made at flow velocities listed in Table 1. At a velocity of 5 ft/sec. the Reynolds number, based on the diameter of the circular entrance to the model, is 2.5×10^4. The pipe diameter Reynolds

number for the BLRF test section at 100°F is 1.2×10^4. Thus, at the lowest measurement velocity, the Reynolds number in the open jet is about twice the Reynolds number in the BLRF test section.

Flow visualization pictures taken with the smoke wire at position 1 are presented in Figure 4 for flow velocities of 10, 15, 20 ft/sec. At 10 and 15 ft/sec., Figure 4 shows that the flow is laminar. However, at 20 ft/sec., some turbulent flow is evident in the lower boundary layer. With the wire located at position 2, flow visualizations are pictured in Figure 5 for 5, 10, 15 ft/s. At 5 and 10 ft/sec. the flow appears laminar. At 15 ft/sec., some turbulence appears in the lower boundary, similar to the flow at position 1. Flow visualization pictures are given in Figure 6 for flow velocities of 5 and 10 ft/sec. at position 3. The flow appears laminar at 5 ft/sec, but at 10 ft/sec. turbulence appears in the top and bottom boundary layers.

Turbulence appears between 5 and 10 ft/sec. where the cross-section is expanding and between 15 and 20 ft/sec. where the cross-section is contracting. Contraction produces accelerating flow and expansion decelerating flow. Turbulence occurs earlier in decelerating flow. At flow velocities of about 5 ft/sec. and less, the flow through the model of the transition section was laminar at all positions. Because the Reynolds number for the model at 5 ft/sec. is nearly twice the Reynolds for the BLRF, it is likely that laminar flow will be maintained through the 3-foot transition section in the BLRF.

2.2.2 Design of Transition and Diffuser Section

The diffuser section is a mirror image of the transition section, so that they share a common design. The design of the transition section was generated by specifying the contour of the inner surface at every three inches along the length of the section. A wooden mandrel was fabricated to match these contours and sanded smooth to form the inside shape of the transition section. The mandrel was coated with relief material. The transition and diffuser sections were fabricated around the mandrel with stainless steel flanges at each end. The flanges contain O-ring grooves for sealing and bolt holes for mounting each section into the BLRF. The contour of the inner surface of the flanges are defined by the inner surface of the circular cross-section in the BLRF or the cross-sectional surface of the new test section. With the flanges in place, the wooden mandrel was coated with a sandable jell-coating which was covered with several layers of fiberglass until a wall thickness of one-half inch was obtained. The mandrel was removed by collapsing it inside the fabricated section by pulling plugs out from the center of the mandrel. A sketch of the transition section is presented in Figure 7.

Every three inches along the length of the transition section, the cross-sectional contour of the inner surface was specified by mathematically locating points on the contour as illustrated in the sketch in Figure 8. Because of the symmetry about both vertical and horizontal planes through the centerline of the section, only one-fourth of the contour was mapped, as shown in Figure 8. The mapping began with the contour at the test section

end of the transition section (left end in Figure 8). Twenty points on the flat part of this contour and ninety points on the circular part of this contour were generated. Corresponding points on the contour three inches from the end were then generated. This process was repeated until the entire transition section was mapped. For each point on the contour at the test section end of the transition section, corresponding points on the cross-sectional contours are connected in Figure 8 with a dashed line. The mathematical algorithms used to generate cross-sectional contours are presented in Appendix C. These algorithms were designed to provide smooth surfaces in the streamwise direction at the entrance and exit of the transition section and to cause every fluid particle to experience changes in the cross-sectional area which are nearly identical and smooth in the streamwise direction. Eight of the cross-sectional contours for the transition and diffuser sections are illustrated in Figure 9.

2.3 Design of Test Section

To accommodate a long flat plate, the cross-section of the test section has been designed with two semi-circles separated by straight lines. To assure laminar flow, the surfaces of the test section must be smooth. Therefore, the finish in the current BLRF test section (16 micro-inch rms finish) was specified. With this finish, laminar flow can be maintained through the 25-foot BLRF circular test section. This required honing the inner surfaces of the new test section which, with the non-circular cross section, would have required special tooling and prohibitive expenditures. Therefore, the test section was fabricated in four pieces so that the surface of each piece could be finished separately. The top and bottom pieces contained the two semi-circular cross sections. These pieces are separated by two flat pieces, one containing the test plate and the other the windows for measurement accessibility by lasers to the fluid flow over the test plate.

An exploded stretch of the major pieces in the test section is presented in Figure 10. A cross-sectional view of the test section is given in Figure 11. The semi-circular portions of the cross-section of the test section are contained in the upper and lower rails. To avoid a discontinuity in the inner surface at the junction of the rails with the test plate and laser window frame, complete semi-circles are required in the two rails. With complete semi-circles, the surfaces are tangent to the flat surfaces of the test section and laser window frame. Before cutting the circular hole out of the sold stainless steel block, the block was cut in half. The halves were clamped together, an 8.44-inch diameter hole cut out of the center, and the surface honed to at least a 16 micro-inch rms finish. The rails were trepanned to assure that the rails remained straight. The stainless steel was annealed prior to machining to relieve internal stresses that could cause bowing.

The test plate is attached to a mounting bracket which is located to a frame attached to the rails. The test plate frame and the laser window frame are attached to the rails and permanently sealed by forcing sealing compound in through grooves between the frames and rails. At the ends of the test section, mounting flanges are attached and permanently sealed. Thus, the

rails, frames and flanges form a permanent assembly to which the test plate and laser windows are attached and sealed with O-rings. This allows easy removal and, if required, replacement of the test plate and laser windows. For example, the windows can be removed and modified to install measurement instrumentation or windows with different shapes used to modify the flow.

3.0 Background Vibration

Measurements were conducted to quantify the reductions in the BLRF background vibration levels required for low wavenumber TBL measurements and identify sources of background vibration in the BLRF test section. Next, treatment to reduce background vibration levels were identified and designed. The reductions in the background vibration levels and vibration measurements conducted on the BLRF are described in Reference 8. A summary of the results from this reference is given in Sections 3.1 and 3.2.

3.1 Reductions of Background Vibration Levels

To specify the background vibration levels required in the BLRF for valid measurements of low wavenumber TBL pressure fluctuation spectral measurements to be made using the flat plate in the new test section, comparisons of estimated background vibration levels in the test plate were made to estimates of the vibration levels of the plate produced by TBL pressure fluctuations. The TBL-induced vibrations constitute the signal in the measurements and background vibrations the noise. There are two sources of background vibrations in the test plate; 1) vibrations in the test section that couple to the test plate and 2) acoustic noise in the test section that excites the test plate into vibration.

Estimates of test plate vibration levels produced by TBL pressure fluctuations, background acoustic noise and background vibrations are presented in Figure 12. The estimated vibration levels due to background vibrations are the average of vibration levels measured on the BLRF test section. Here, it is assumed that the levels in the test plate caused by background vibration in the new test section will be equal to the background vibration levels measured on the current BLRF test section. This is conservative since 1) the junction between the test plate and new test section will provide some vibration attenuation, 2) the new test section will be more massive than the existing test section, and thereby less susceptible to vibration excitation, and 3) the array of accelerometers used in the low wavenumber TBL measurements will partially reject background vibrations in the test plate. However, since it is desirable to reduce the background vibration levels to below the expected signal levels, the vibration levels measured on the current BLRF test section should provide a valid guideline for estimating required reductions in background vibration levels in the test plate due to the background vibrations in the new test section.

Both the TBL- and acoustically-induced vibration levels were estimated by ignoring the effects of the boundaries of the test plate. Therefore, the estimated levels are mean values of the levels as a function of frequency [9]. At resonances, the levels will be higher and at anti-resonances the levels will be lower than the estimated levels. Since all of the levels will

be subject to the same fluctuations between resonances and anti-resonances, the comparisons given in Figure 12 can be used to provide estimates of required vibration reduction.

The TBL-induced vibration levels shown in Figure 12 were estimated by summing the product of the TBL wall pressure fluctuation spectrum and the square of the admittance of an 1/8-inch thick infinite steel plate over all wavenumbers. The TBL wavenumber pressure fluctuation spectrum was estimated using the Corcos model [10]. The frequency spectra of the TBL pressure fluctuations were taken from measurements conducted in the BLRF [11]. The admittance of the test plate was modeled as the inverse of the sum of the wavenumber/frequency impedances of an infinite elastic plate and the glycerine at the surface of the plate [12].

The acoustically-induced vibration levels shown in Figure 12 were estimated by summing the product of the square of the admittance of an infinite fluid-loaded 1/8-inch plate and acoustic spectrum over all wavenumbers up to the acoustic wavenumbers. The sum was taken only up to the acoustic wavenumber because all of the acoustic noise inside the test section will propagate along the plate at or above the acoustic phase speed. The acoustic spectrum measured in the BLRF with laminar flow in the test section was used in making the estimates of acoustically-induced vibration levels of the test plate.

As shown in Figure 12, the acoustically-induced vibration levels are much lower than the TBL-induced vibration levels so that it is unlikely that the acoustic background noise in the modified BLRF will be a source of vibrations in the new test plate that will interfere with the low wavenumber TBL spectral measurements. Therefore, no treatment of the acoustic noise has been included in the modifications of the BLRF. However, if direct pressure measurements are made in the modified BLRF, then a reassessment of the acoustic background noise may be required.

Figure 12 shows that reductions of up to approximately 40 dB will be required in the background vibrations of the new BLRF test section to assure that valid low wavenumber TBL pressure spectral measurements can be made with the test plate in the new test section. Using diagnostic measurements, the sources of the background vibrations in the BLRF test section are identified in Section 3.2. Treatments for the reduction of background vibrations are described in Section 3.3.

3.2 Sources of Background Vibrations

Figure 13 shows vibration levels measured at different locations on the BLRF with the BLRF running. As expected, the highest vibration levels occur below the pump. Levels at the opposite end of the lower leg of the BLRF are lower than the levels measured in the middle of the test section. This indicates that the pump and motor driving the pump are primary sources of background vibrations in the test section. This conclusion is supported by coherence measurements taken between the vibrations on the middle of the test section and vibrations of the pump and motor (See Figure 14). The pump in

the heat exchanger, used to control the temperature and thereby the Reynolds numbers of the flow in the BLRF, is another source of background vibrations as shown in Figure 15. At frequencies above 225 Hz, vibration levels in the test section generated by the heat exchanger pump are nearly equal to the levels generated by the BLRF pump and motor. Because the BLRF is located near the 48-inch water tunnel, operation of the 48-inch water tunnel is another potential source of vibration. Vibration levels measured at the location of the base of the BLRF closest to the 48-inch water tunnel are shown in Figure 16 with the BLRF running and the 48-inch tunnel off, and with the BLRF off and the 48-inch tunnel on. Above 200 Hz, the vibration levels at the base of the BLRF generated by the 48-inch water tunnel are nearly equal to the levels generated by sources in the BLRF.

Conclusions drawn based on the data presented in Figure 13 through 16, as well as from other data presented in Reference 8, are:

1) As expected, the primary sources of test section background vibrations in the BLRF are the pump and drive motor, so that reductions of the pump/motor vibrations and attenuation of the vibration from the pump/motor to the test section are required to reduce background vibration levels in the new test plate.

2) The heat exchanger pump/motor is a source of vibration in the test section that will require reduction to provide the vibration reductions shown in Figure 12.

3) Vibration generated by sources outside the BLRF, such as the 48-inch water tunnel, must be reduced to provide the reductions in the vibration levels shown in Figure 12. Since these sources are difficult to control, the only viable approach left is to reduce the transmission of the vibrations from outside sources into the BLRF.

Other measurements, reported in Reference 8, show that cavitation in the pump, if present, is not a significant source of acoustic background noise. Vibration measurements on the test section showed little attenuation from one end of the test section to the other. No clear direction of propagation of the vibrations in the test section could be identified from vibration phase measurements. Both of these results indicate that the vibrations in the test section are highly reverberant with little internal attenuation. Also, unsteady pressure measurements made in the test section by flush-mounted transducers showed little attenuation along the length of the test section. This is expected since the cutoff frequency for the test section is about 26 Hz; only plane wave propagation occurs in the test section and plane waves suffer little attenuation.

As a part of another research program in the BLRF, a plastic section was installed in the upstream end of the BLRF test section. Because the vibration attenuation in plastic is likely to be higher than in stainless steel, the installation of the plastic section in the BLRF provided an opportunity to investigate vibration reduction in the test section associated with attenuation of vibration transmission in the BLRF walls between the

pump/motor and test section. Averages of the vibration levels measured by accelerometers on the test section before and after installation of the plastic section are presented in Figure 17. Above 250 Hz, reductions of nearly 10 dB occurred. This indicates that resilient sections in the BLRF walls will produce reductions in the BLRF wall vibrations.

3.3 Vibration Reduction Treatments

To reduce the vibrations generated by the pump/motor, the pump impeller was balanced, the impeller blade surfaces smoothed, and the shafts of the pump and motor aligned. A flexible shaft coupling was installed between the pump and motor to reduce vibrations induced by misalignment and transmission of vibrations from the motor to the pump. The motor was mounted on resilient mounts to reduce the transmission of motor vibrations to the pump and BLRF through the foundation common to the pump and motor.

Because the pump is located just upstream of the upstream elbow of the lower leg of the BLRF (See Figure 18), the space required to vibration isolate the pump from the BLRF is not available. Isolation of the pump would have required moving the pump with a major redesign of the lower leg. Because of the costs involved and the need to be able to restore the BLRF to its original configuration so that current boundary layer research can be continued, isolation of the pump was not included in the vibration reduction treatments of the BLRF.

The remaining vibration reduction treatments added to the BLRF are designed to increase vibration attenuation along the vibration transmission paths from the source to the receiver. Since the receiver is the test plate in the test section, the treatments are placed between the test section and the sources of vibration, which have been identified as the BLRF pump/motor, the heat exchanger pump/motor, and outside sources coupled to the BLRF by common support structures. Two vibration transmission path treatments are employed in the modification to the BLRF; vibration isolation and vibration damping. Vibration isolation treatments consist of resilient elements placed along the vibration transmission path to decouple the receiver from the sources. Damping treatments are designed to dissipate the vibrational energy as it propagates along the transmission path from the source to the receiver.

To isolate the test section from pump vibrations, flexible boots were installed in the two vertical legs that separate the upper horizontal leg with the test section from the lower horizontal leg with the pump. As shown in Figure 18, installation of these boots required that the upper leg be raised. Also, because the flexible boots cannot support the upper leg, new supports for the upper leg were required. As illustrated in Figure 18, a two-stage resilient mounting system has been used to support the upper leg and vibration isolate the new test section in the upper leg from vibrations in the foundation under the BLRF to which the two-stage mounting system is attached. The two-stage resilient mounting system was not attached to the lower leg, as are the present upper leg supports, to avoid coupling the lower leg of the BLRF with the primary sources of vibration, i. e. the pump and motor, to the test section. To maximize the effectiveness of the two-stage mounting system, the impedances of the upper and lower resilient mounts

should be as close to being equal as possible and the mass of the raft between the resilient mounts near the mass of the mounted structure, which is 10,000 lbs. [13]. To meet the first criterion, the same types of mounts were used above and below the rafts. Large concrete blocks, used as rafts, have a combined weight of approximately 8,000 lbs. In addition to vibration isolation of the upper leg of the BLRF, the lower leg is vibration isolated from the foundation by the resilient mounts shown in Figure 18 under the lower leg. To avoid nullifying the effectiveness of the lower leg resilient mounts, a flexible boot was installed between the pump, which is hard mounted to the foundation, and the resiliently mounted lower leg.

The vibration isolation treatments of the heat exchanger pump are shown in Figure 19. The foundation for the pump, reduction gear and motor is resiliently mounted to the beam structure that also supports the BLRF. In addition, resilient elements were installed into the piping that connects the heat exchanger pump to the BLRF and to the heat exchanger located under the BLRF.

Damping treatments are added to the outside surfaces of the modified BLRF as shown in Figure 18. Because the path length from the pump to the test section in the direction opposite the flow is small and the frequencies where vibration reduction is required are low (below 500 Hz), the number of wavelengths along the treated path will not be large. Since the effectiveness of the damping depends on the number of wavelengths along the damped path and the damping loss factor, the loss factor of the treatment had to be maximized to provide an effective treatment over the short path available for treatment from the pump to the diffuser section.

To achieve high damping of low frequencies over short paths, a treatment that is a combination of cut constrained layer damping and passive dynamic absorber was designed. Since the low frequency damping of cut constrained layer damping treatments is high [14] and cut constrained layers can be configured as a dynamic absorber with the elements in the cut constraining layer providing the mass and the damping layer providing the stiffness, it was the basis for the design of the vibration reduction treatment.

The cut constrained layer damping/dynamic absorber treatment is illustrated in a section view in Figure 20. Motion of the supporting structure (e.g., the wall of the BLRF) will be transmitted through the resilient damping layer to the elements in the cut constraining layer. If the mass of the elements in the cut constraining layer and the stiffness of the damping layer are tuned to provide dynamic absorption at the first resonant frequency of the BLRF, then significant reduction in the vibration at the first resonance can be achieved. At resonant frequencies above the first resonant frequency, the high damping provided by the cut constrained layer damping treatment will provide significant reductions in vibration levels by damping resonant responses as well as dissipating energy along the transmission path. At nonresonant frequencies, the vibration reduction produced by damping must rely on energy dissipation along the transmission path. Although the losses will not be as large as the losses at the resonant frequencies, the losses should be adequate because the vibration levels of the untreated BLRF are lower at the nonresonant frequencies.

Using the procedures described in Appendix D, 1/8 by 4-in., one foot long aluminum constraining layer plates over 0.05 in. Dyad damping material was selected for use on the outer walls of the nontest sections of the BLRF shown in Figure 18.

4.0 Summary

The Penn State Boundary Layer Research Facility (BLRF) has been modified so that low wavenumber turbulent boundary layer (TBL) wall pressure spectra can be measured. The BLRF test section was redesigned to accommodate the long flat plate to be used as a transducer in these measurements. Also, extensive treatments to reduce the background vibration levels in the new test section were added to the BLRF. An increase in the measurement accessibility to the boundary layer was included in the design of the new BLRF test section. With these modifications, the BLRF possesses the following properties:

1) Because the working medium is glycerine, a thick boundary layer with large eddy structures when the layer is turbulent,

2) Low background vibration levels in the test section,

3) Measurement accessibility to a large area of the boundary layer,

4) An exchangeable elastic test plate in contact with the boundary layer, and

5) Control of laminar, transition and turbulent boundary layer flow.

With these properties, the modified BLRF not only is a unique facility for the measurement of low wavenumber TBL spectral levels, but also a unique facility for a wide range of experimental research on boundary layer/structure interaction.

References

[1] W. K. Blake and D. M. Chase, "Wavenumber-Frequency Spectra of Turbulent Boundary Layer Pressure Measured by Microphone Arrays," J. Acoust. Soc. Am., 49, pp. 862-877 (1971).

[2] T. M. Farabee and F. E. Geib, Jr., "Measurement of Boundary Layer Pressure Fields with an Array of Pressure Transducers in a Subsonic Flow," Proc. Int. Congr. Intrum. Aerospace Facil, 6th, Ottawa, Canada, pp. 311-319 (1975).

[3] F. E. Geib, Jr. and T. M. Farabee, "Measurement of Boundary Layer Pressure Fluctuations at Low Wavenumber on Smooth and Rough Walls," David W. Taylor Naval Ship R&D Center, Rep. No. 84-05, Washington DC, (1985).

[4] N. C. Martin and P. Lechey, "Low Wavenumber Wall Pressure Measurements Using a Rectangular Membrane as a Spectral Filter," J. Sound Vibr. 52(1) pp. 95-120 (1977).

[5] P. W. Jameson, "Measurement of the Low-Wavenumber Component of Turbulent Boundary Layer Pressure Spectral Density," Proc. Symp. Turbul. Liq., 4th, pp. 192-200 (1975).

[6] E. H. Kennard, "The New Approach to Shell Theory: Circular Cylinders," J. Appl. Mech. 20, pp. 33-40 (1953).

[7] Werner Soedel, "Vibrations of Shells and Plates," Marial Decker Inc., New York, (1981).

[8] C. B. Burroughs, "Background Noise and Vibration in the Boundary Layer Research Facility," ARL Penn State TN 86-203, 26 November 1986.

[9] Eugene Skudrzyk, "The Mean-Value Method of Predicting the Dynamic Response of Complex Vibrators," J. Acoust, Soc. Am. 67(4), pp. 1105-1135 (April 1980).

[10] G. M. Corcos, "Resolution of Pressure in Turbulence," J. Acoust. Soc. Am. 35(2), pp. 192-199 (Feb. 1963).

[11] Gerald C. Lauchle and Mark A. Daniels, "Wall-Pressure Fluctuations in Turbulent Pipe Flow," The Physics of Fluids 30(10), pp. 3019-3024 (Oct. 1987).

[12] Miguel C. Junger and David Feit, "Sound, Structures, and Their Interaction," 2nd. Edition, The MIT Press, Cambridge, MA, (1986).

[13] E. E. Ungar and C. W. Dietrich, "High-Frequency Vibration Isolation," J. Sound Vibra. 4(2), pp. 224-241 (1966).

[14] G. G. Parfett, "The Effect of Cuts in Damping Tapes," Fourth Intern Congress on Acoust., Paper P21, Copenhagen, (21-25 August 1962).

[15] J. C. Snowdon, "Vibration and Shock in Damped Mechanical Mechanical Systems,"John Wiley and Sons, New York, NY (1968).

[16] A. D. Nashif, DIG Jones and J. P. Henderson, "Vibration Damping," John Wiley and Sons, New York, NY (1885).

SMOKE WIRE POSITION*	FLOW VELOCITIES (ft/s)
1	10, 15 and 20
2	5, 10 and 25
3	5 and 10

* See Figure 3

TABLE 1. SMOKE WIRE FLOW VISUALIZATION MEASUREMENTS IN THE TRANSITION SECTION MODEL

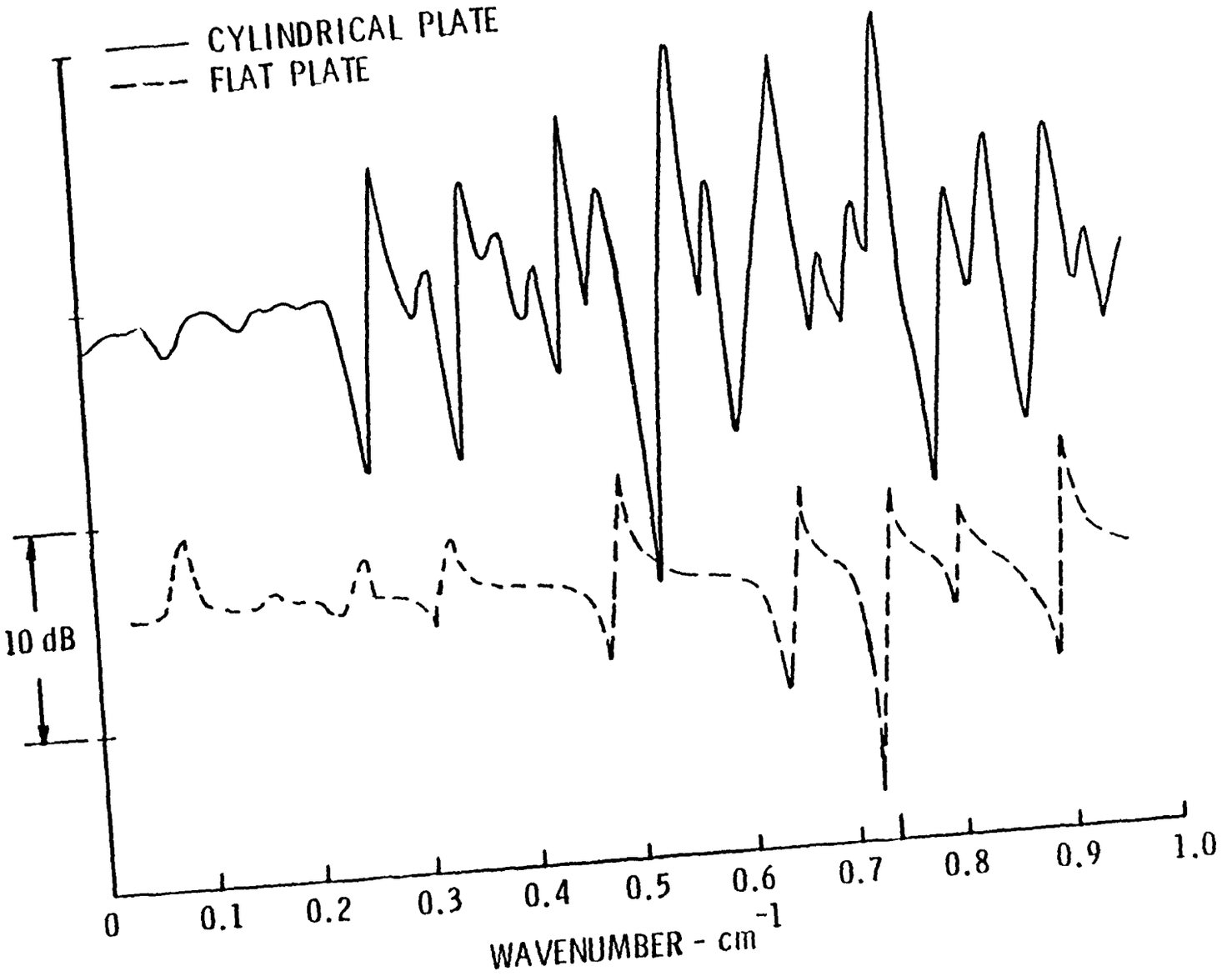

FIGURE 1. WAVENUMBER DRIVE IMPEDANCES FOR CYLINDRICAL AND FLAT PLATES AT 100Hz

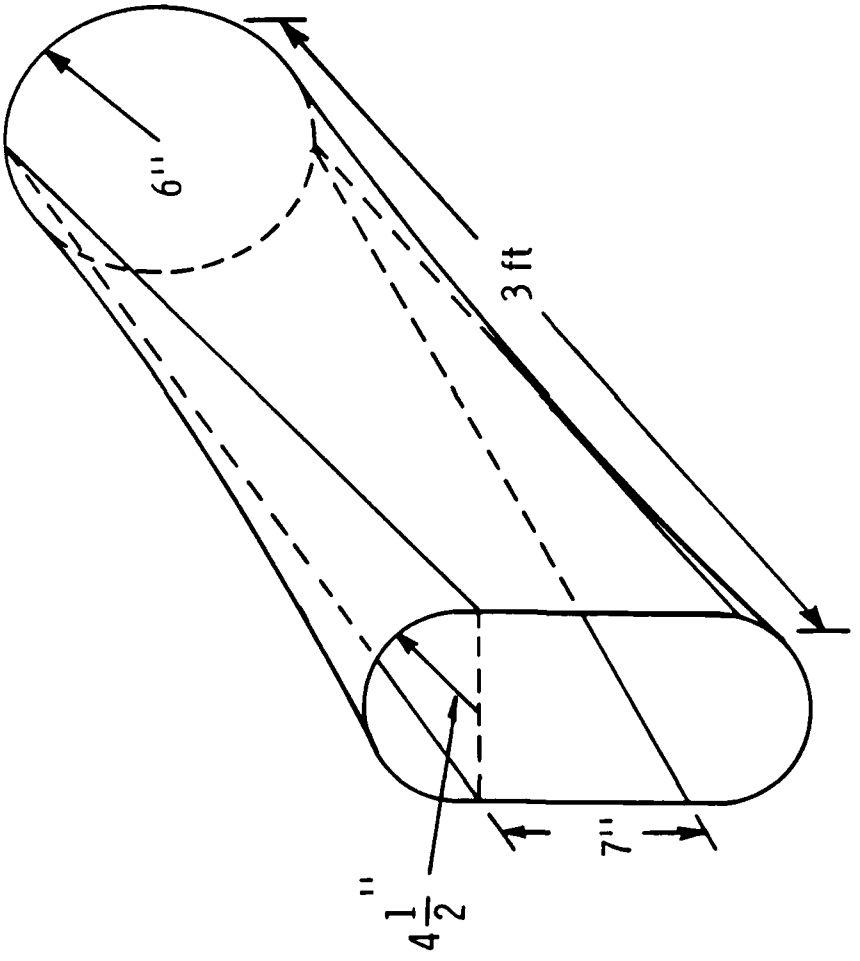

FIGURE 2. SKETCH OF SHEET METAL MODEL OF TRANSITION SECTION

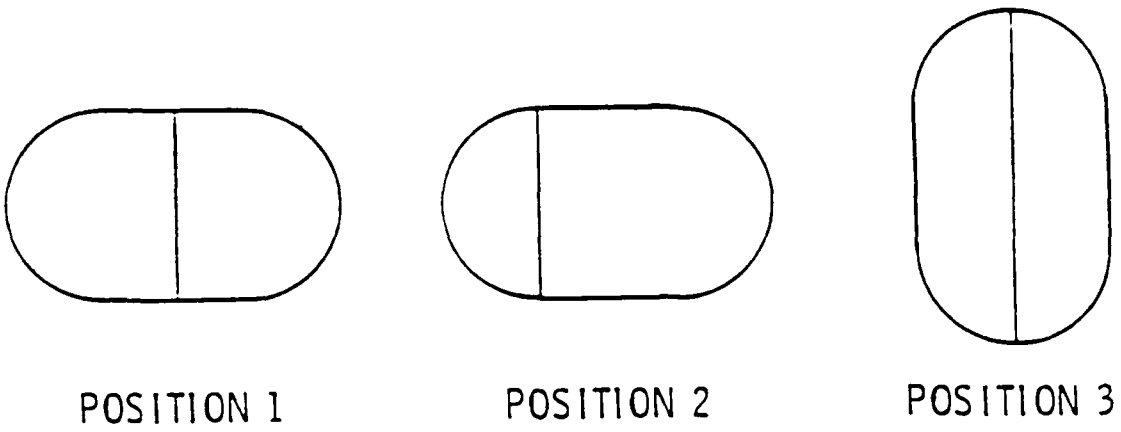

FIGURE 3. SMOKE WIRE FLOW VISUALIZATION POSITIONS OF THE EXIT TO THE TRANSITION SECTION MODEL

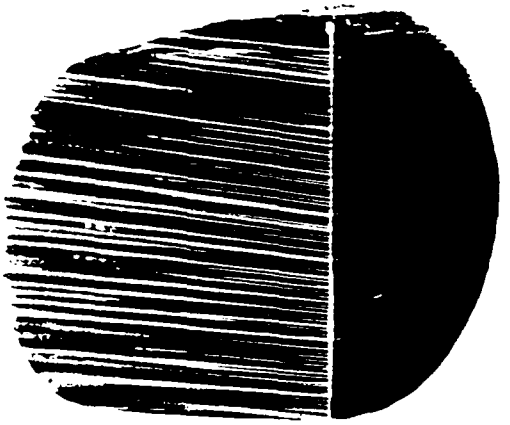

FLOW VELOCITY

10 ft/s

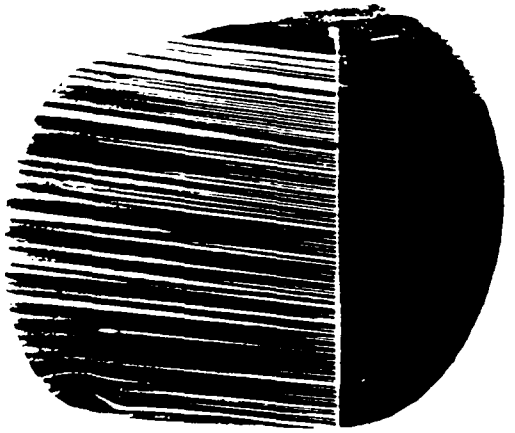

15 ft/s

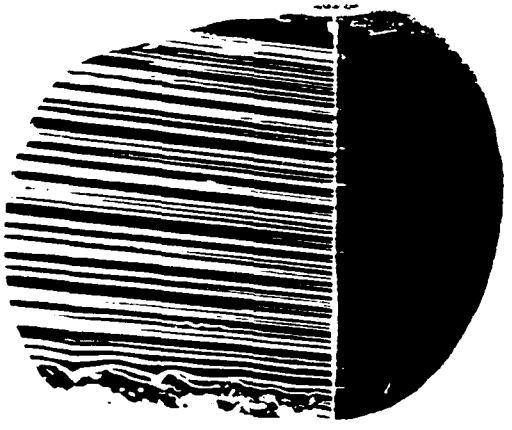

20 ft/s

FIGURE 4. FLOW VISUALIZATION PICTURES WITH SMOKE WIRE AT POSITION 1 (SEE FIGURE 3) FOR FLOW VELOCITIES OF 10 ft/sec. (TOP), 20 ft/sec. (BOTTOM)

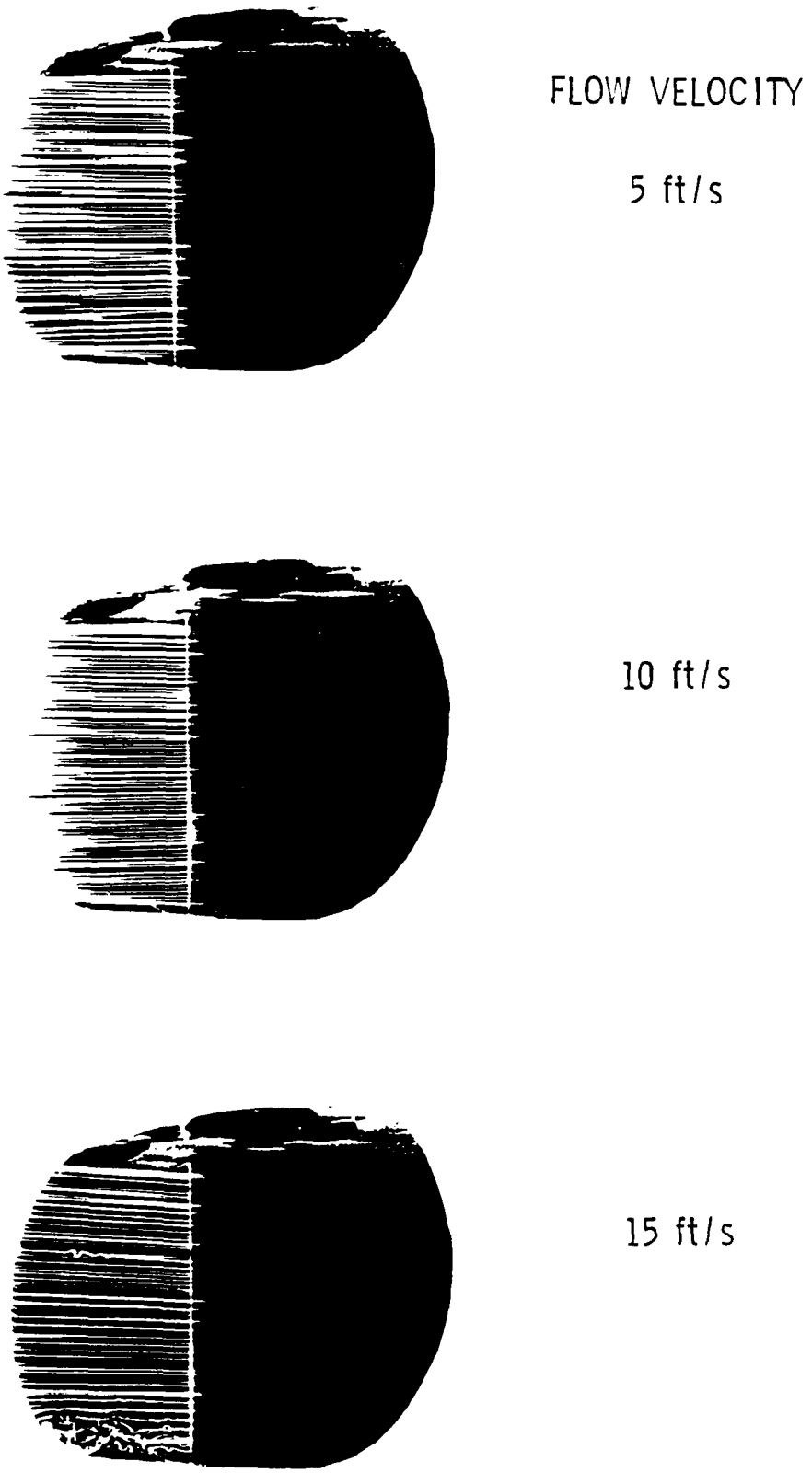

FIGURE 5. FLOW VISUALIZATION PICTURES WITH SMOKE WIRE AT POSITION 2 (SEE FIGURE 3) FOR FLOW VELOCITIES OF 5 ft/sec. (TOP), 10 ft/sec. (MIDDLE) AND 15 ft/sec. (BOTTOM)

FLOW VELOCITY

10 ft/s

5 ft/s

FIGURE 6. FLOW VISUALIZATION PICTURES WITH SMOKE WIRE AT POSITION 3 (SEE FIGURE 3) FOR FLOW VELOCITIES OF 10 ft/sec. (TOP), AND 5 ft/sec. (BOTTOM)

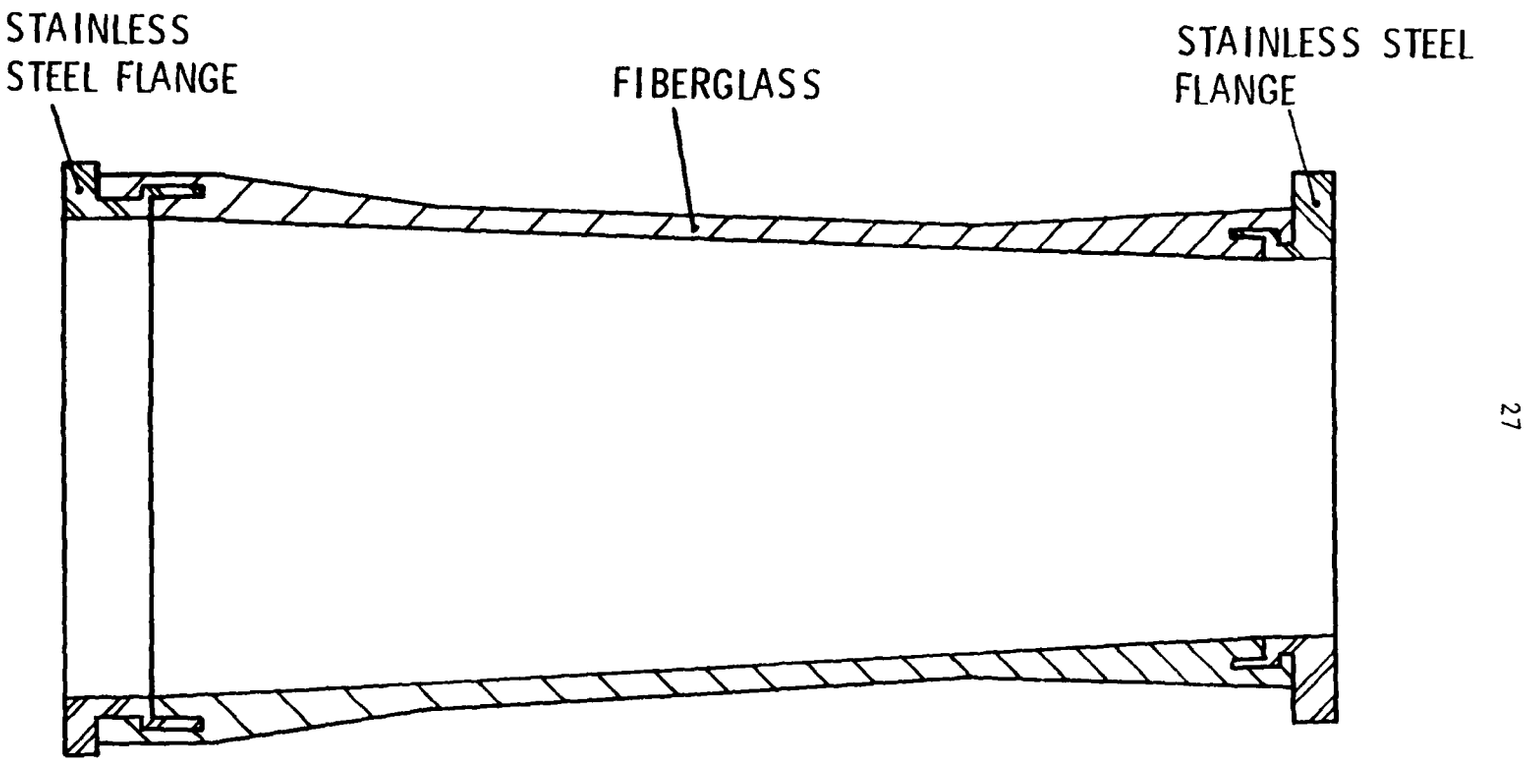

FIGURE 7. TRANSITION SECTION

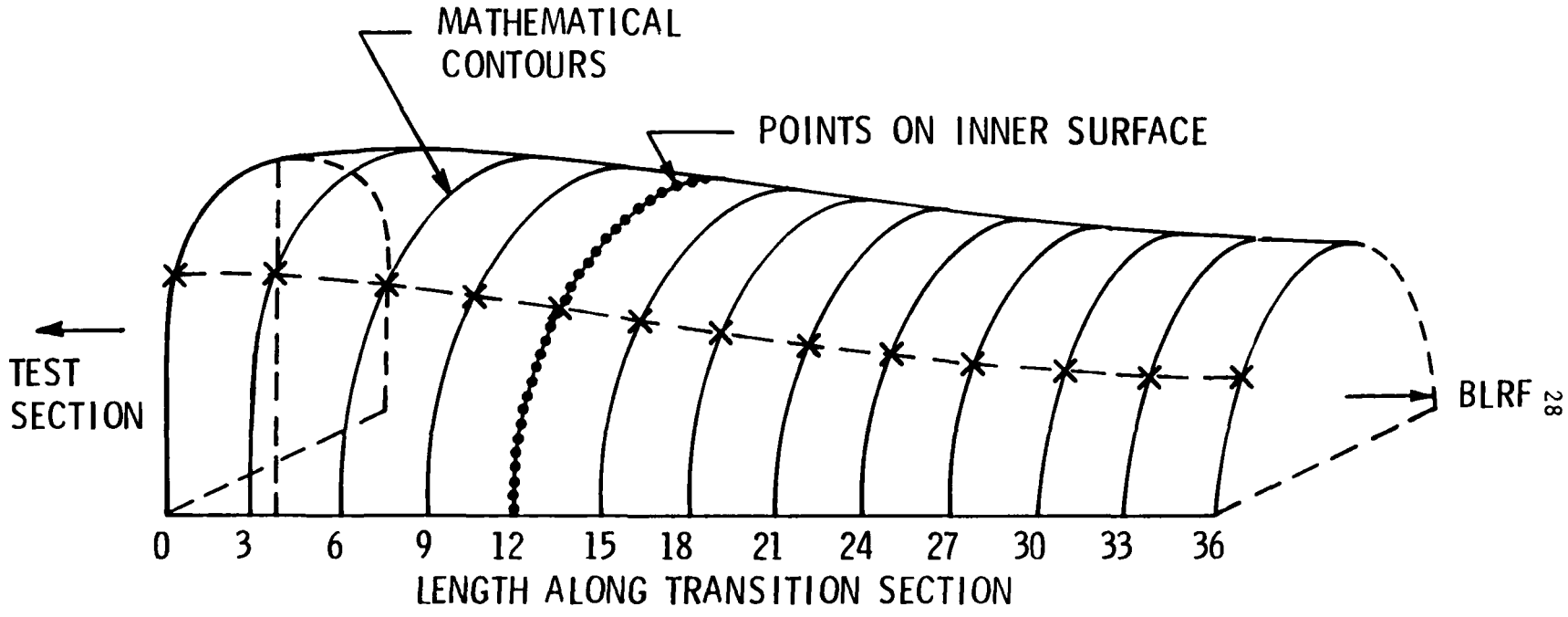

FIGURE 8. MAPPING OF INNER SURFACE OF TRANSITION SECTION

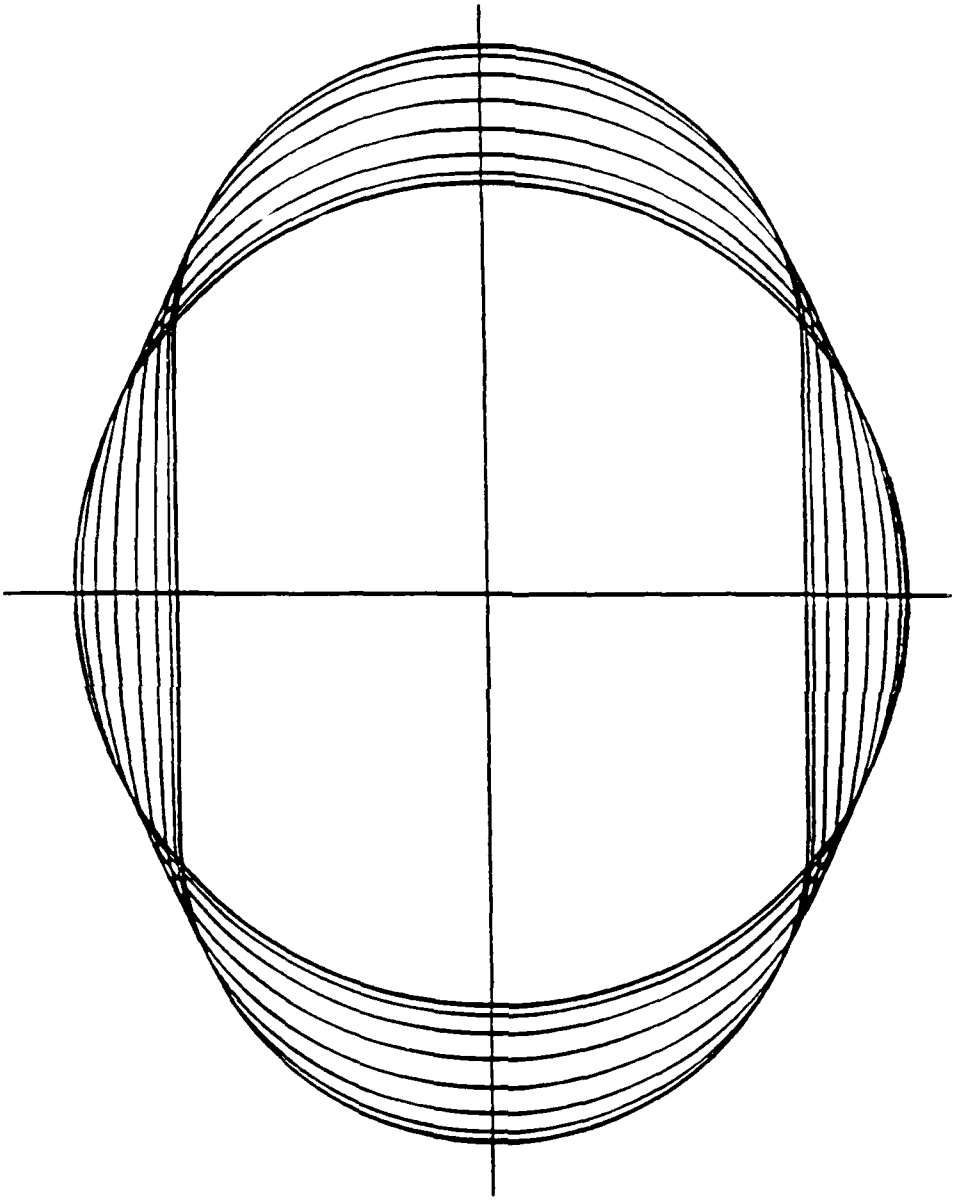

FIGURE 9. CROSS SECTIONAL COUNTOURS OF INNER SURFACE OF TRANSITION SECTION

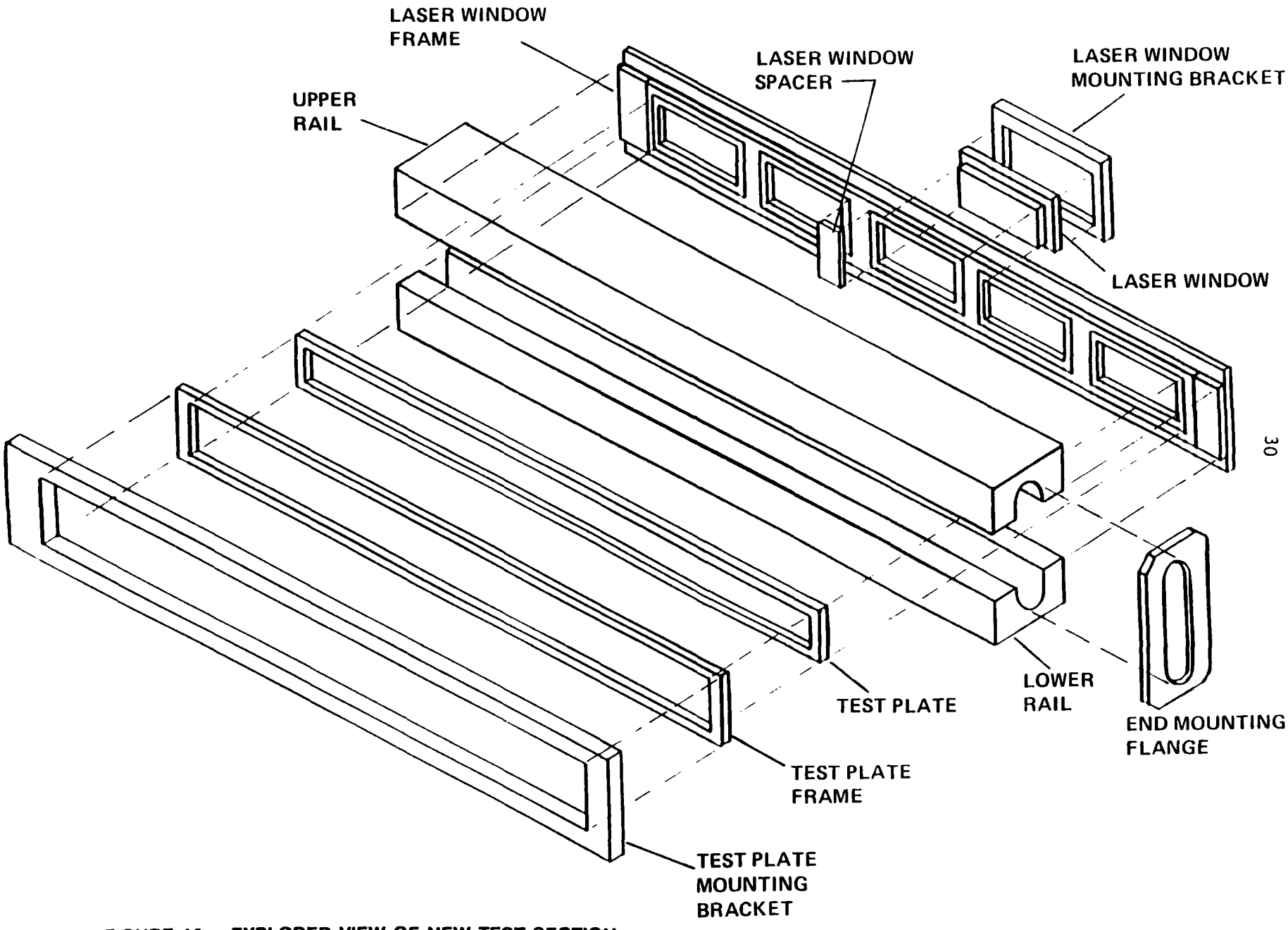

FIGURE 10. EXPLODED VIEW OF NEW TEST SECTION

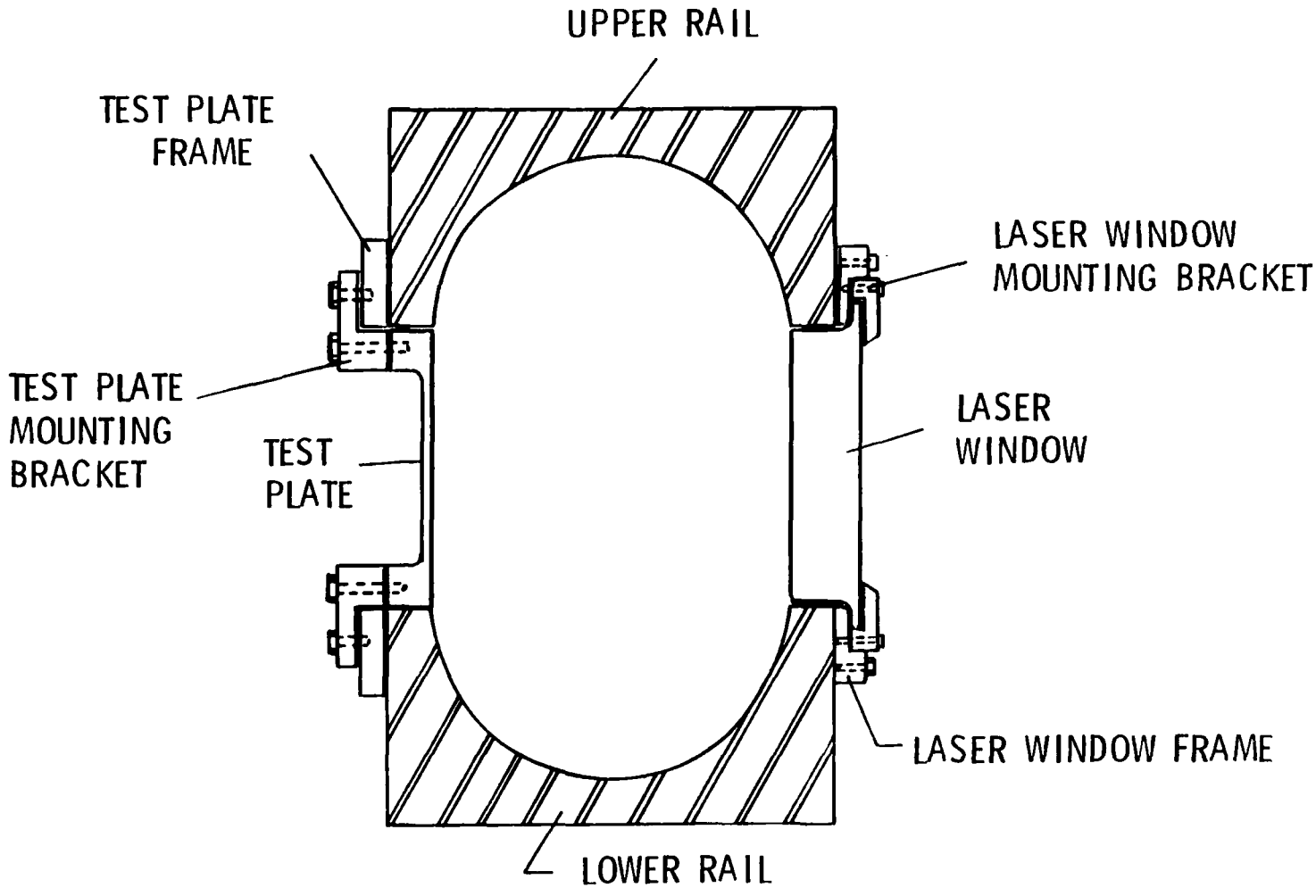

FIGURE 11. CROSS SECTION OF NEW BLRF TEST SECTION

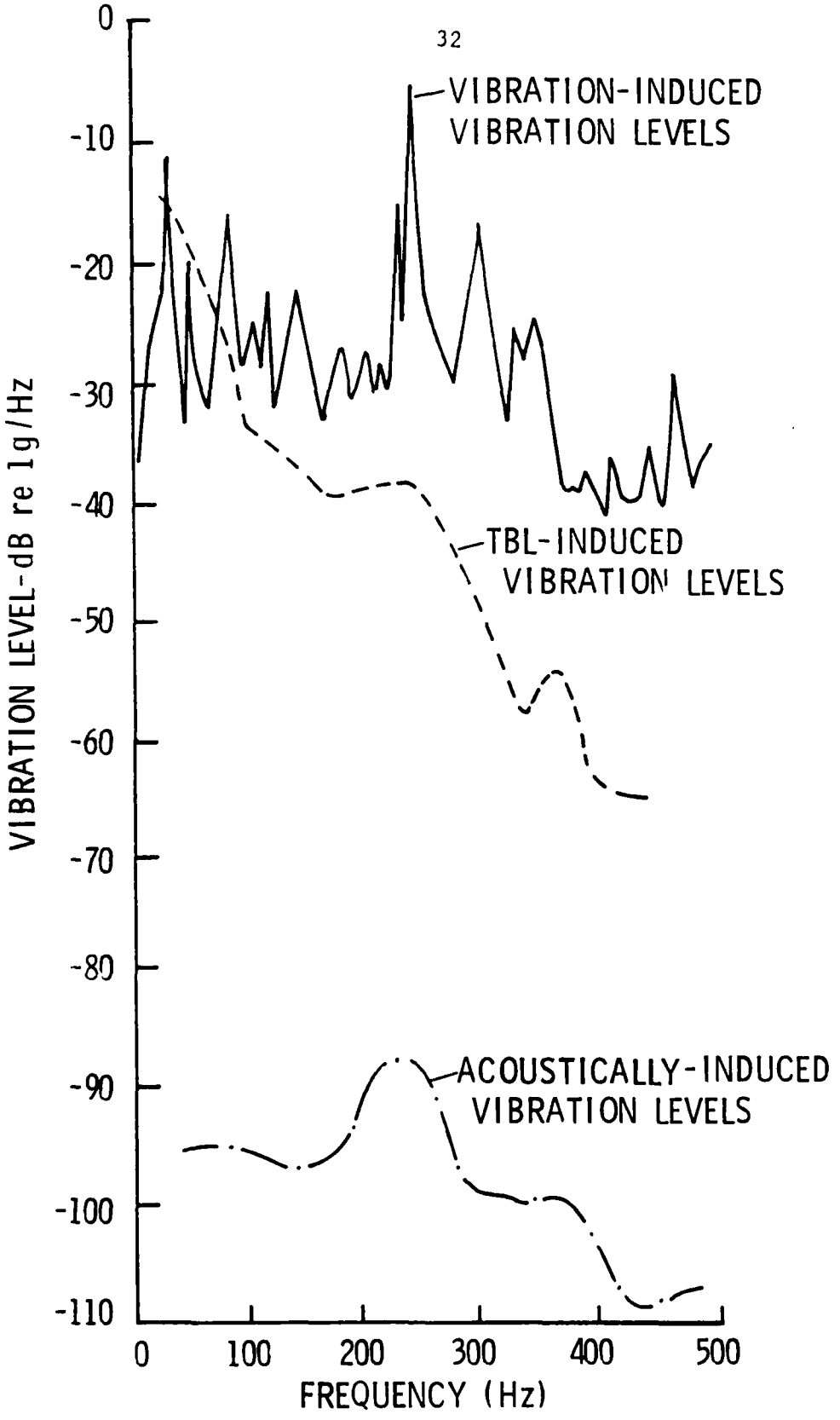

FIGURE 12. ESTIMATED VIBRATION LEVELS OF THE NEW TEST PLATE GENERATED BY BACKGROUND VIBRATIONS, ACOUSTIC NOISE, AND TURBULENT BOUNDARY LAYER PRESSURE FLUCTUATIONS

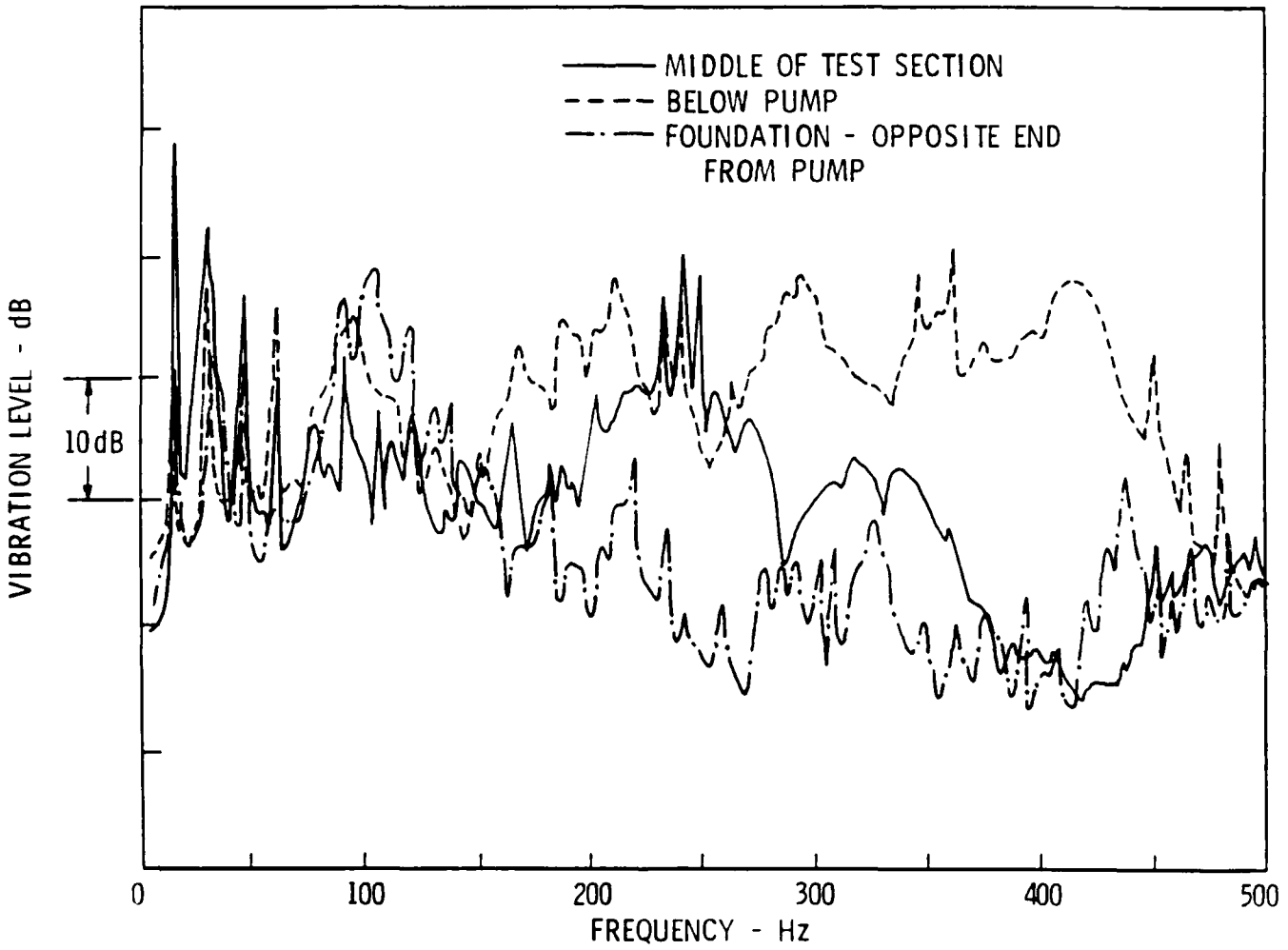

FIGURE 13. MEASURED VIBRATION LEVELS AT DIFFERENT LOCATIONS AROUND THE BLRF

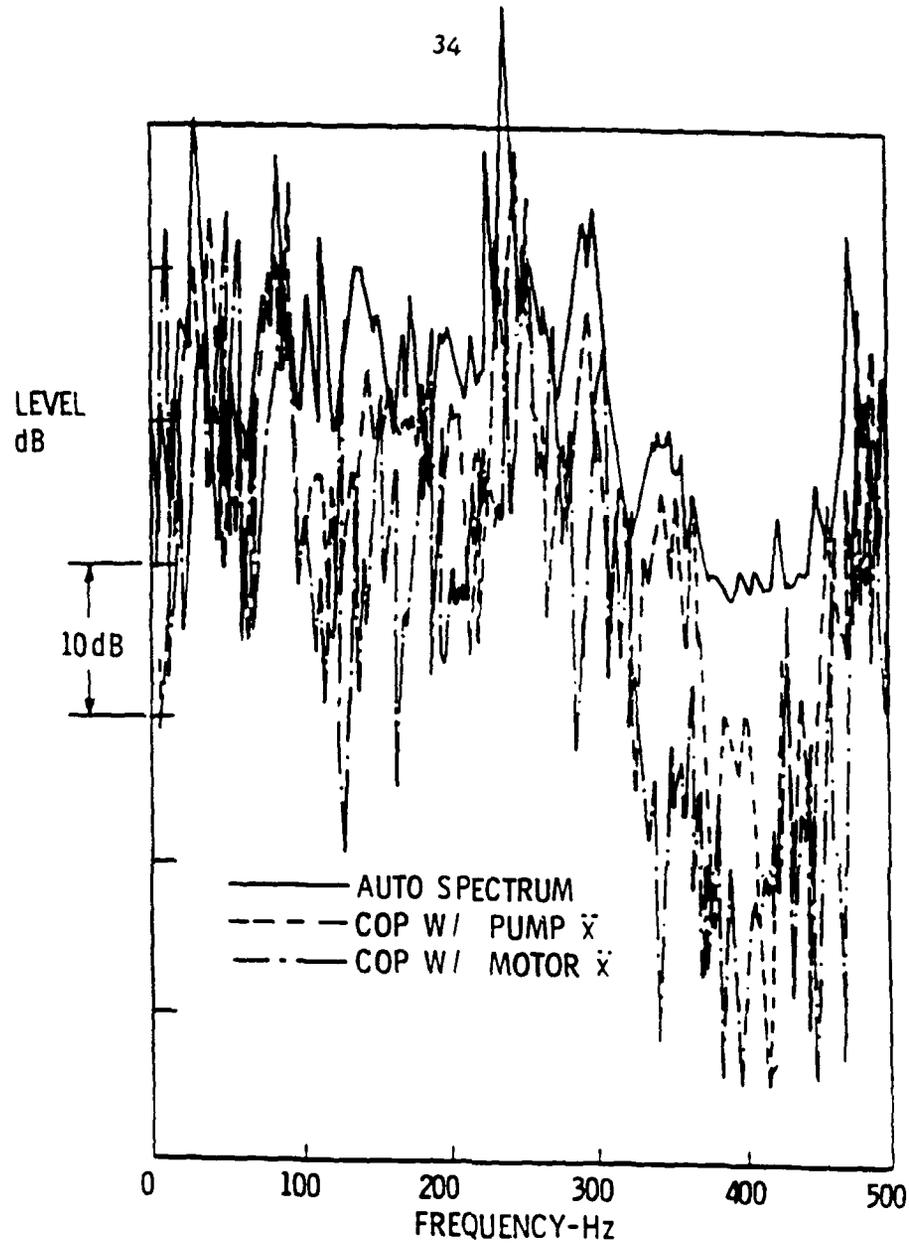

FIGURE 14. AUTO SPECTRAL AND COHERENT OUTPUT POWER VIBRATION LEVELS IN THE MIDDLE OF THE TEST SECTION WITHOUT THE FLEXIBLE COUPLING AND WITH THE TRIP RING

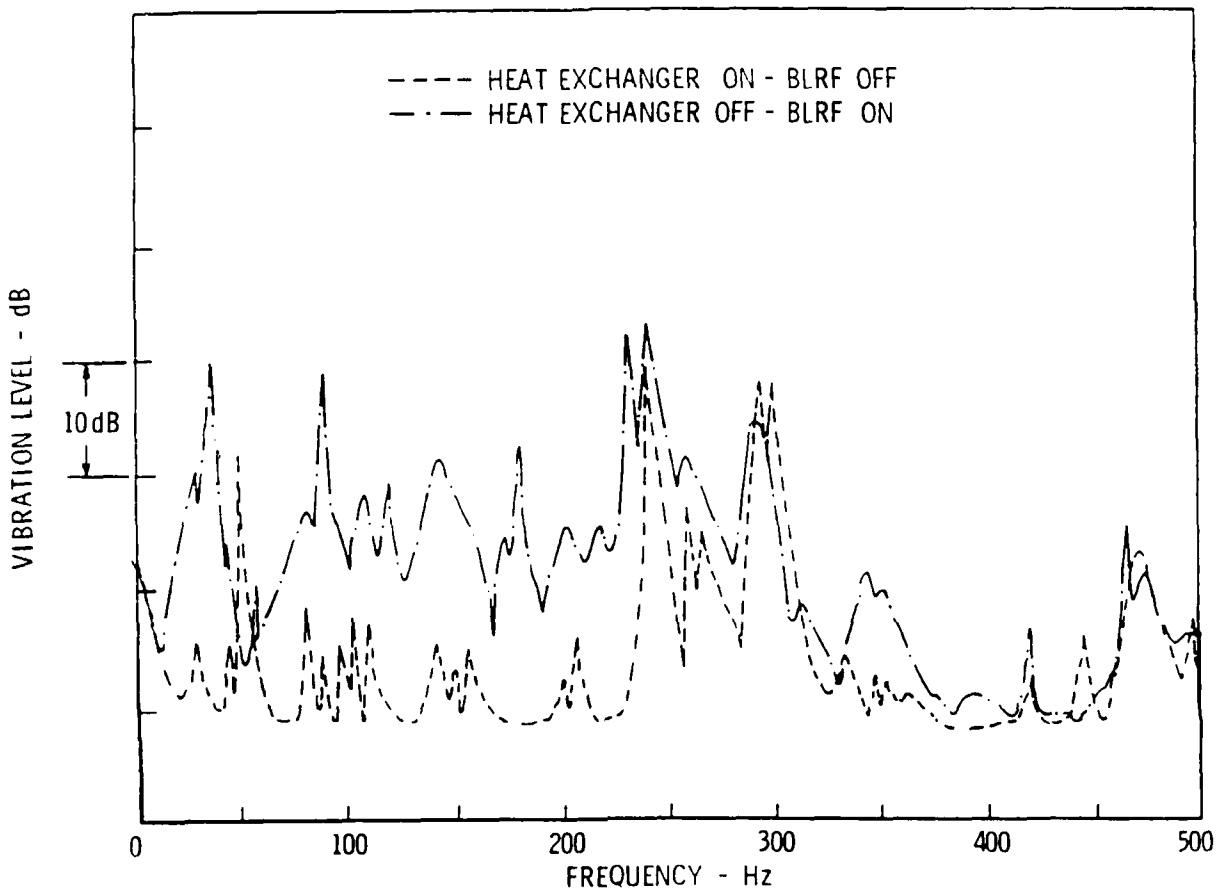

FIGURE 15. MEASURED VIBRATION LEVELS IN THE MIDDLE OF THE TEST SECTION WITH AND WITHOUT THE BLRF AND/OR HEAT EXCHANGER RUNNING

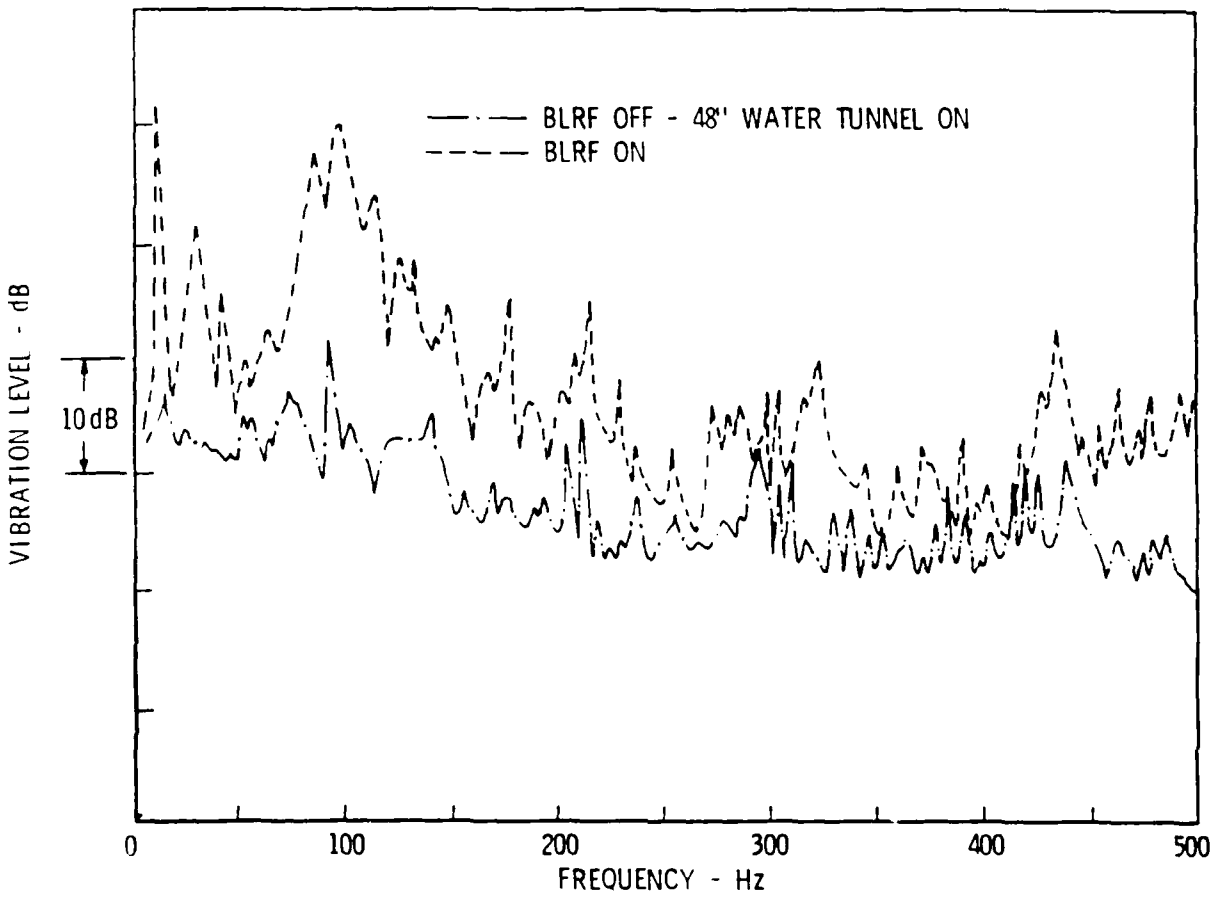

FIGURE 16. MEASURED VIBRATION LEVELS AT THE BASE OF THE BLRF NEAR THE LARGE WATER TUNNEL WITH AND WITHOUT THE BLRF AND/OR THE LARGE WATER TUNNEL RUNNING

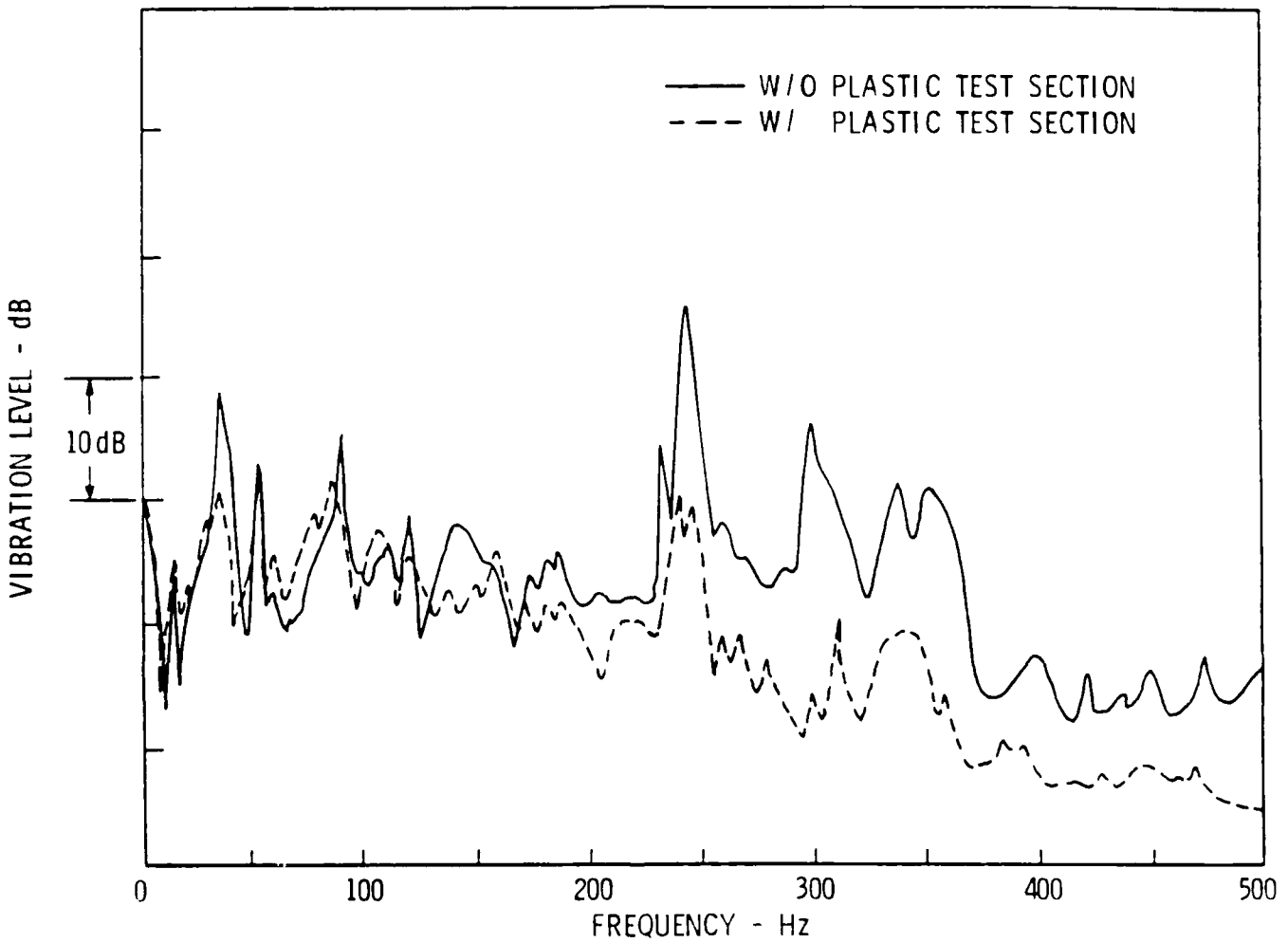

FIGURE 17. AVERAGE OF MEASURED VIBRATION LEVELS IN THE MIDDLE OF THE BLRF TEST SECTION WITH AND WITHOUT THE PLASTIC TEST SECTION IN THE DOWNSTREAM END OF THE BLRF TEST SECTION

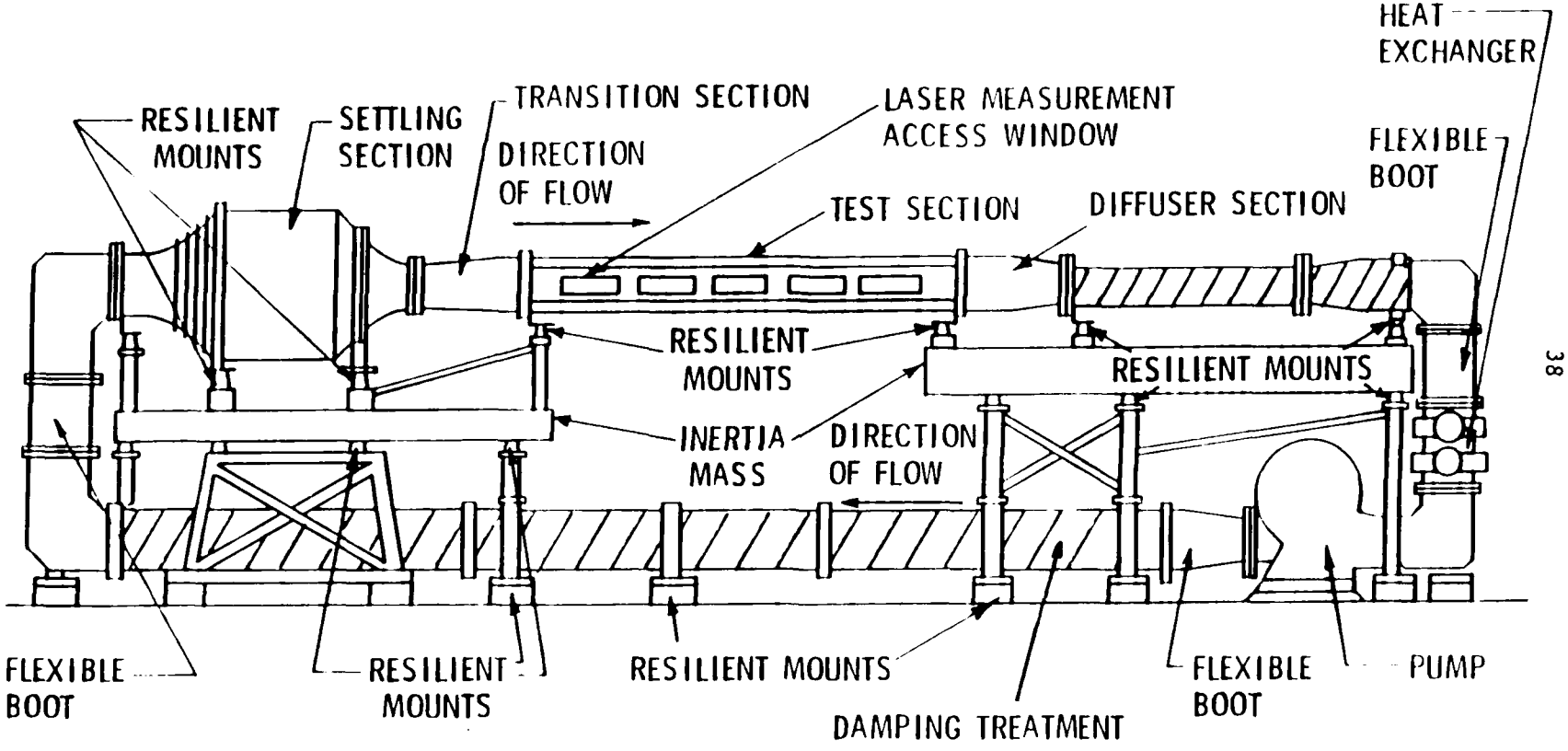

FIGURE 18. NOISE TREATMENTS AND NEW TEST SECTION FOR BLRF

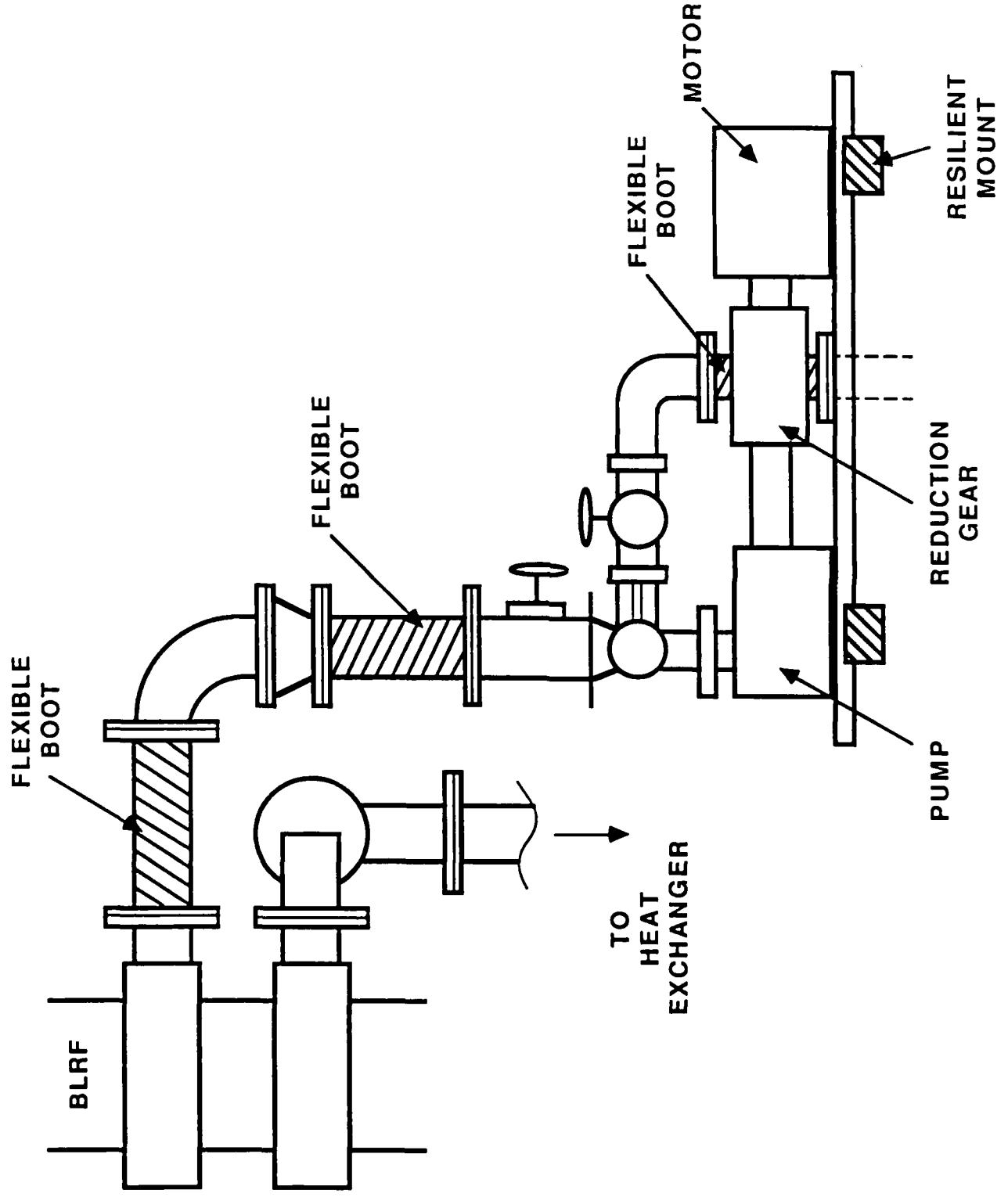

FIGURE 19. VIBRATION ISOLATION OF THE HEAT EXCHANGE PUMP

CBB-289-13

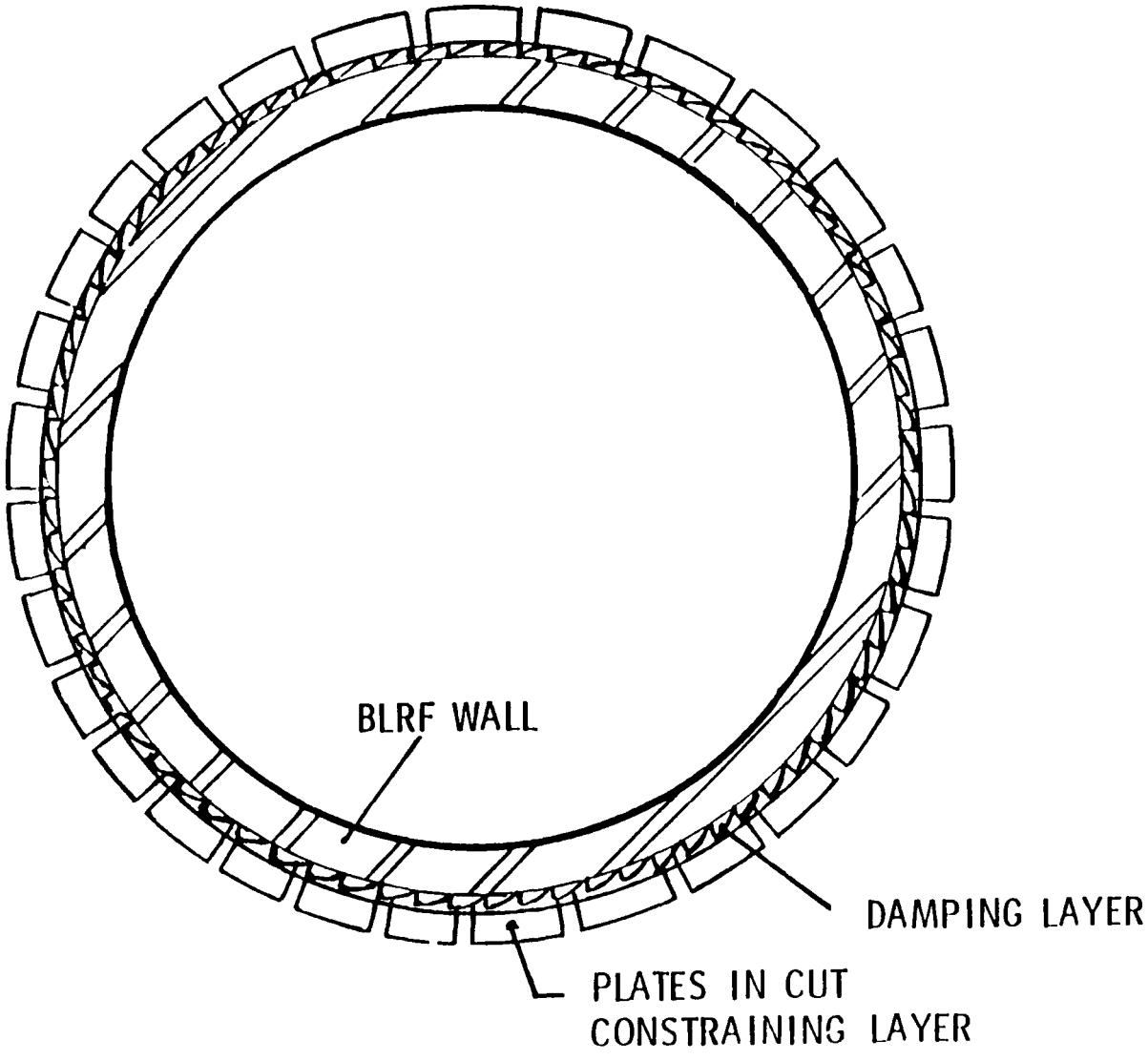

FIGURE 20. CUT CONSTRAINED LAYER DAMPING TREATMENT ON BLRF

Appendix A

WAVENUMBER DRIVE IMPEDANCE MODEL FOR FLAT AND CYLINDRICAL PARTS

In cylindrical shell theory, the radial displacements are coupled to the two in-plane axial and circumferential displacements by means of three coupled differential equations. Therefore, three boundary conditions tied to each of the three displacement variables are required. For displacements small compared to the thickness, plate theory involves only one independent variable, i.e. the radial displacement, which means that only one boundary condition along each edge is required. Therefore, developing equations for the boundary conditions that are applicable to both the cylindrical shell and flat plate are difficult. The conditions on the in-plane displacements required for the cylindrical shell are not included in the plate theory. To avoid this problem, the cylindrical shell theory is used to model both the cylindrical and flat plate. The flat plate is modeled by letting the radius of the cylindrical plate approach a large value while maintaining the width of the plate constant.

The governing differential equations for a circular cylindrical shell are [6]

$$\frac{\partial^2 u}{\partial x^2} + \frac{1-\nu}{2a^2}\frac{\partial^2 u}{\partial \phi^2} + \frac{1+\nu}{2a}\frac{\partial^2 v}{\partial x \partial \phi} + \frac{\nu}{a}\frac{\partial w}{\partial x} + k_p^2 u = 0$$

$$\frac{1+\nu}{2a}\frac{\partial^2 u}{\partial x \partial \phi} + \frac{1}{a^2}\frac{\partial^2 v}{\partial \phi^2} + \frac{1-\nu}{2}\frac{\partial^2 v}{\partial x^2} + \frac{1}{a^2}\frac{\partial w}{\partial \phi} + \frac{h^2\nu}{8(1-\nu)a^4}\left(\frac{\partial w}{\partial \phi} + \frac{\partial^3 w}{\partial \phi^3}\right) + k_p^2 v = 0 \qquad \text{(A-1)}$$

$$\frac{\nu}{a}\frac{\partial u}{\partial x} + \frac{1}{a^2}\frac{\partial v}{\partial \phi} + \frac{w}{a^2} + \frac{h^2}{24(1-\nu)}\left[2(1-\nu)\left(\frac{\partial^2}{\partial x^2} + \frac{1}{a^2}\frac{\partial^2}{\partial \phi^2}\right)w + \frac{4-\nu}{a^4}\frac{\partial^2 w}{\partial \phi^2}\right] + \frac{2+\nu}{a^4}w - k_p^2 w = -i\omega K f_a(x,\phi)$$

where u, v and w are the axial in-plane, circumferential in-plane and radial velocities, respectively, x and ϕ are the cylindrical coordinates in the axial and circumferential directions, respectively, ν is Poisson's constant, a is the radius of the shell middle surface, h is the thickness of the shell, $k_p = \omega/C_e$, where $C_e = [E/\rho(1-\nu^2)]^{1/2}$ is the longitudinal wave speed, ρ is the volume density of the shell material, E is Young's modulus of the shell material and $K = \frac{a^2}{\rho C_e^2}\left[\frac{1}{h} + \frac{1-2\nu}{2a(1-\nu)}\right]$. The external applied pressure is given in equation (A-1) by $f_a(x,\phi)$.

Since the test plate in the BLRF will be long in the streamwise direction (x-direction), the conditions at the up and down stream ends (x=constant) will have limited impact on the response of the plate so we can model the plate as infinite in the x-direction. This permits us to take the Fourier transform of equation (A-1) on x,

$$(\Omega^2 - \alpha^2)u + \frac{1-\nu}{2}\frac{\partial^2 u}{\partial\phi^2} + i\alpha\left(\frac{1+\nu}{2}\right)\frac{\partial v}{\partial\phi} + i\alpha\nu w = 0$$

$$i\alpha\left(\frac{1+\nu}{2}\right)\frac{\partial u}{\partial\phi} + \left(\Omega^2 - \alpha^2\frac{1-\nu}{2}\right)v + \frac{\partial^2 v}{\partial\phi^2} + \frac{\partial w}{\partial\phi} + \frac{h^2\nu}{8(1-\nu)a^2}\left(\frac{\partial w}{\partial\phi} + \frac{\partial^3 w}{\partial\phi^3}\right) = 0 \qquad \text{(A-2)}$$

$$i\alpha\nu u + \frac{\partial v}{\partial\phi} + (1-\Omega^2)w + \frac{h^2}{24a^2(1-\nu)}\left[2(1-\nu)\left(\frac{\partial^2}{\partial\phi^2} - \alpha^2\right)^2 + (4-\nu)\frac{\partial^2 w}{\partial\phi^2}\right] + (2+\nu)w = -i\omega K f_a(k,\phi)$$

where $u = u(k,\phi)$, $v = v(k,\phi)$, $w = w(k,\phi)$, k is the wavenumber, $\alpha = ka$ and $\Omega = a\omega/C_e$. For an external pure wavenumber drive with a width δ in the ϕ direction

$$f_a(k,\phi) = F\delta(k-k_d)H(\phi-\phi_d) \qquad \text{(A-3)}$$

where

$$H(\phi-\phi_d) = \begin{cases} 0 & |\phi-\phi_d| > \delta \\ \dfrac{1}{2\delta} & |\phi-\phi_d| < \delta \end{cases} \qquad \text{(A-4)}$$

In the above equation, ϕ_d is the center of the drive width and k_d is the wavenumber of the drive in the x-direction. For a drive of infinitesimal width $[F\delta(k-k_d)\delta(\phi-\phi_d)]$, the solutions given in this appendix do not converge. Using equation (A-3) in equation (A-2) and assuming $h/a \ll 1$ yields

$$(\Omega^2 - \alpha^2)u + \frac{1-\nu}{2}\frac{\partial^2 u}{\partial\phi^2} + i\alpha\left(\frac{1+\nu}{2}\right)\frac{\partial v}{\partial\phi} + i\alpha\nu w = 0 \qquad \text{(A-5)}$$

$$i\alpha\left(\frac{1+\nu}{2}\right)\frac{\partial u}{\partial\phi} + \left(\Omega^2 - \alpha^2\frac{1-\nu}{2}\right)v + \frac{\partial^2 v}{\partial\phi^2} + \frac{\partial w}{\partial\phi} = 0 \qquad \text{(A-6)}$$

$$i\alpha\nu u + \frac{\partial v}{\partial\phi} + (1-\Omega^2)w = -i\omega K F\delta(k-k_d)H(\phi-\phi_d) \qquad \text{(A-7)}$$

Solving equation (A-7) for u and substituting into equations (A-5) and (A-6) yields

$$-\left[\Omega^2 - \alpha^2 + \left(\frac{1+\nu}{2}\right)\alpha^2\nu\right]\frac{\partial v}{\partial \phi} - \left[(\Omega^2-\alpha^2)(1-\Omega^2) + \alpha^2\nu^2\right]w - \left(\frac{1-\nu}{2}\right)\frac{\partial^3 v}{\partial \phi^3} \qquad \text{(A-8)}$$

$$-\left(\frac{1-\nu}{2}\right)\left(1-\Omega^2\right)\frac{\partial^2 w}{\partial \phi^2} = i\omega(\Omega^2-\alpha^2)KF\delta(k-k_d)\frac{\partial^2}{\partial \phi^2}H(\phi-\phi_d)$$

$$-\left[\frac{1+\nu}{2\nu} - 1\right]\frac{\partial^2 v}{\partial \phi^2} - \left[\left(\frac{1+\nu}{2\nu}\right)\left(1-\Omega^2\right) - 1\right]\frac{\partial w}{\partial \phi} + \left(\Omega^2 - \alpha^2\frac{1-\nu}{2}\right)v \qquad \text{(A-9)}$$

$$= i\omega\left(\frac{1+\nu}{2\nu}\right)KF\delta(k-k_d)\frac{\partial}{\partial \phi}H(\phi-\phi_d)$$

As illustrated in Figure A-1, the edges in the x-direction (ϕ=constant) are modeled as simply supported where

$$w = 0, \quad N_{\phi\phi} = 0, \quad M_{\phi\phi} = 0 \qquad \text{(A-10)}$$

at $\phi = \pm \phi_e$, where $N_{\phi\phi}$ is the in-plane stress resultant and $M_{\phi\phi}$ the moment resultant in the ϕ-direction. The moment resultant is given by [7].

$$M_{\phi\phi} = \frac{D}{i\omega}\left[\frac{1}{a^2}\left(\frac{\partial v}{\partial \phi} - \frac{\partial^2 w}{\partial \phi^2}\right) - \frac{\partial^2 w}{\partial x^2}\right] \qquad \text{(A-11)}$$

where $D = \dfrac{Eh^3}{12(1-\nu^2)}$ is the bending stiffness. Since $\dfrac{\partial^2 w}{\partial x^2} = 0$ along the rigid simple support, equation (A-11) becomes

$$\frac{\partial v}{\partial \phi} - \frac{\partial^2 w}{\partial \phi^2} = 0 \qquad \text{(A-12)}$$

The normal stress resultant is [7]

$$N_{\phi\phi} = \frac{K}{i\omega}\left[\frac{1}{a}\frac{\partial w}{\partial \phi} + \frac{w}{a} + \nu\frac{\partial u}{\partial x}\right] \qquad \text{(A-13)}$$

where $K = \dfrac{Eh}{1-\nu^2}$ is the membrane stiffness. Again, for rigid simple supports $\dfrac{\partial u}{\partial x} = 0$, so that equation (A-13) becomes

$$\frac{\partial w}{\partial \phi} + w = 0 \qquad \text{(A-14)}$$

Thus, the boundary conditions become

$$w = 0$$

$$\frac{\partial v}{\partial \phi} - \frac{\partial^2 w}{\partial \phi^2} = 0 \qquad \text{(A-15)}$$

$$\frac{\partial w}{\partial \phi} + w = 0$$

The above boundary conditions are satisfied by solutions of the form

$$w(k,\phi) = \sum_n \left\{ A_n(k) \sin\left(\frac{n\pi\phi}{\phi_e}\right) + A_n'(k) \cos\left(\frac{2n+1}{2}\,\pi\,\frac{\phi}{\phi_e}\right) \right\}$$

$$v(k,\phi) = \sum_n \left\{ B_n(k) \cos\left(\frac{n\pi\phi}{\phi_e}\right) + B_n'(k) \sin\left(\frac{2n+1}{2}\,\pi\,\frac{\phi}{\phi_e}\right) \right\} \qquad \text{(A-16)}$$

Substituting equation (A-16) into equation (A-8)

$$\begin{aligned}
&\sum_n \left\{ A_n(k) \left[-(\Omega^2-\alpha^2)(1-\Omega^2) - \alpha^2\nu^2 + \left(\frac{1-\nu}{2}\right)\left(1-\Omega^2\right)\left(\frac{n\pi}{\phi_e}\right)^2 \right] \right. \\
&\quad \left. + B_n(k) \left[\Omega^2 - \alpha^2 + \left(\frac{1+\nu}{2}\right)\alpha^2\nu \right]\left(\frac{n\pi}{\phi_e}\right) - \left(\frac{1-\nu}{2}\right)\left(\frac{n\pi}{\phi_e}\right)^3 \right\} \sin\left(\frac{n\pi\phi}{\phi_e}\right) \\
&\quad + \sum_n \left\{ A_n'(k) \left[-(\Omega^2-\alpha^2)(1-\Omega^2) - \alpha^2\nu + \left(\frac{1-\nu}{2}\right)\left(1-\Omega^2\right)\left(\frac{2n+1}{2\phi_e}\,\pi\right)^2 \right] \right. \\
&\quad + B_n'(k) \left[-\left(\Omega^2-\alpha^2 + \left(\frac{1+\nu}{2}\right)\alpha^2\nu\right)\left(\frac{2n+1}{2\phi_e}\,\pi\right) \right. \\
&\quad \left. \left. + \left(\frac{1-\nu}{2}\right)\left(\frac{2n+1}{2\phi_e}\,\pi\right)^3 \right] \right\} \cos\left(\frac{2n+1}{2}\,\pi\,\frac{\phi}{\phi_e}\right) \\
&\quad = i\omega(\Omega^2-\alpha^2)KF\delta(k-k_d)H(\phi-\phi_d) + i\omega\left(\frac{1-\nu}{2}\right)KF\delta(k-k_d)\frac{\partial^2}{\partial\phi^2}H(\phi-\phi_d)
\end{aligned} \qquad \text{(A-17)}$$

where $A_n(k)$, $A_n'(k)$, $B_n(k)$ and $B_n'(k)$ are functions to be determined.

Operating on equation (A-17) with $\int_{-\phi_e}^{\phi_e} \sin\left(\frac{m\pi\phi}{\phi_e}\right) d\phi$ yields

$$A_m(k) \bigwedge_{11}^{m}(k) + B_m(k) \bigwedge_{12}^{m}(k) = \frac{i\omega F}{\phi_e} K\delta(k-k_d)\left[\Omega^2 - \alpha^2 - \left(\frac{1-\nu}{2}\right)\left(\frac{m\pi}{\phi_e}\right)^2\right] \sin\left(\frac{m\pi\phi_d}{\phi_e}\right) \frac{\sin\left(\frac{m\pi\delta}{\phi_e}\right)}{\left(\frac{m\pi\delta}{\phi_e}\right)} \tag{A-18}$$

where

$$\bigwedge_{11}^{m}(k) = -(\Omega^2 - \alpha^2)(1-\Omega^2) - \alpha^2\nu^2 + \left(\frac{1-\nu}{2}\right)(1-\Omega^2)\left(\frac{m\pi}{\phi_e}\right)^2$$

$$\bigwedge_{12}^{m}(k) = \left[\Omega^2 - \alpha^2 + \left(\frac{1+\nu}{2}\right)\alpha^2\nu\right]\left(\frac{m\pi}{\phi_e}\right) - \left(\frac{1-\nu}{2}\right)\left(\frac{m\pi}{\phi_e}\right)^3 \tag{A-19}$$

Operating on equation (A-17) with $\int_{-\phi_e}^{\phi_e} \cos\left(\frac{2m+1}{2}\,\pi\,\frac{\phi}{\phi_e}\right) d\phi$ yields

$$A_m'(k) \bigwedge_{11}^{m'}(k) + B_m'(k) \bigwedge_{12}^{m'}(k) = \frac{i\omega F}{\phi_e} K\delta(k-k_d)\left[\Omega^2 - \alpha^2 - \left(\frac{1-\nu}{2}\right)\left(\frac{2m+1}{2\phi_e}\,\pi\right)^2\right] \cos\left(\frac{2m+1}{2}\,\pi\,\frac{\phi}{\phi_e}\right) \frac{\sin\left(\frac{2m+1}{2}\,\pi\,\frac{\delta}{\phi_e}\right)}{\left(\frac{2m+1}{2}\,\pi\,\frac{\delta}{\phi_e}\right)} \tag{A-20}$$

where

$$\bigwedge_{11}^{m}(k) = -(\Omega^2 - \alpha^2)(1-\Omega^2) - \alpha^2\nu + \left(\frac{1-\nu}{2}\right)(1-\Omega^2)\left(\frac{2m+1}{2\phi_e}\,\pi\right)^2$$

$$\bigwedge_{12}^{m}(k) = -\left[\Omega^2 - \alpha^2 + \left(\frac{1+\nu}{2}\right)\alpha^2\nu\right]\left(\frac{2m+1}{2\phi_e}\,\pi\right) + \left(\frac{1-\nu}{2}\right)\left(\frac{2m+1}{2\phi_e}\,\pi\right)^3 \tag{A-21}$$

Substituting equations (A-16) into (A-9)

$$\sum_n \left\{ A_n(k) \left[-\left(\frac{1+\nu}{2\nu}\right)\left(1-\Omega^2\right) - 1 \right]\left(\frac{n\pi}{\phi_e}\right) + B_n(k)\left[\left(\frac{1-\nu}{2\nu}\right)\left(\frac{n\pi}{\phi_e}\right)^2 + \left(\Omega^2 - \alpha^2\,\frac{1-\nu}{2}\right)\right]\right\}$$
$$\cos\left(\frac{n\pi\phi}{\phi_e}\right) + \sum_n \left\{ A_n'(k)\left[\left(\frac{1+\nu}{2\nu}\right)\left(1-\Omega^2\right) - 1\right]\left(\frac{2n+1}{2\phi_e}\,\pi\right)\right.$$
$$\left. + B_n'(k)\left[\left(\frac{1-\nu}{2\nu}\right)\left(\frac{2m+1}{2\phi_e}\,\pi\right)^2 + \left(\Omega^2 - \alpha^2\,\frac{1-\nu}{2}\right)\right]\right\}\sin\left(\frac{2n+1}{2}\,\pi\,\frac{\phi}{\phi_e}\right) \tag{A-22}$$
$$= i\omega\left(\frac{1+\nu}{2\nu}\right) FK\delta(k-k_d)\frac{\partial}{\partial\phi}H(\phi-\phi_d)$$

Operating on equation (A-22) with $\int_{-\phi_e}^{\phi_e} \cos\left(\frac{m\pi\phi}{\phi_e}\right)d\phi$ yields

$$A_m(k)\Lambda_{21}^m(k) + B_m(k)\Lambda_{22}^m(k)$$
$$= -\frac{i\omega F}{\phi_e}\left(\frac{1+\nu}{2\nu}\right) K\delta(k-k_d)\left(\frac{m\pi}{\phi_e}\right)\sin\left(\frac{m\pi\phi_d}{\phi_e}\right)\frac{\sin\left(\frac{m\pi\delta}{\phi_e}\right)}{\left(\frac{m\pi\delta}{\phi_e}\right)} \tag{A-23}$$

where

$$\Lambda_{21}^m(k) = -\left[\left(\frac{1+\nu}{2\nu}\right)\left(1-\Omega^2\right) - 1\right]\left(\frac{m\pi}{\phi_e}\right)$$
$$\Lambda_{22}^m(k) = \frac{1-\nu}{2\nu}\left(\frac{m\pi}{\phi_e}\right)^2 + \Omega^2 - \alpha^2\,\frac{1-\nu}{2} \tag{A-24}$$

Operating on equation (A-22) with $\int_{-\phi_e}^{\phi_e} \sin\left(\frac{2m+1}{2}\,\pi\,\frac{\phi}{\phi_e}\right)d\phi$ yields

$$A_m'(k)\Lambda_{21}^{m'}(k) + B_m'(k)\Lambda_{22}^{m'}(k)$$
$$= -\frac{i\omega F}{\phi_e}\left(\frac{1+\nu}{2\nu}\right) K\delta(k-k_d)\left(\frac{2m+1}{2\phi_e}\,\pi\right)\cos\left(\frac{2m+1}{2}\,\pi\,\frac{\phi_d}{\phi_e}\right)\frac{\sin\left(\frac{2m+1}{2}\,\pi\,\frac{\delta}{\phi_e}\right)}{\left(\frac{2m+1}{2}\,\pi\,\frac{\delta}{\phi_e}\right)} \tag{A-25}$$

where

$$\bigwedge_{21}^{m'}(k) = \left[\left(\frac{1+\nu}{2\nu}\right)\left(1-\Omega^2\right) - 1\right]\left(\frac{2m+1}{2\phi_e}\,\pi\right)$$

$$\bigwedge_{22}^{m'}(k) = \left(\frac{1-\nu}{2\nu}\right)\left(\frac{2m+1}{2\phi_e}\,\pi\right)^2 + \Omega^2 - \alpha^2\,\frac{1-\nu}{2} \qquad \text{(A-26)}$$

Solving equations (A-18) and (A-23) for $A_m(k)$

$$A_m(k) = \frac{\dfrac{i\omega F}{\phi_e}\,K\delta(k-k_d)\,\sin\left(\dfrac{m\pi\phi_d}{\phi_e}\right)\dfrac{\sin\left(\dfrac{m\pi\delta}{\phi_e}\right)}{\left(\dfrac{m\pi\delta}{\phi_e}\right)}\,\Gamma_m}{\bigwedge_{11}^{m}(k)\bigwedge_{22}^{m}(k) - \bigwedge_{21}^{m}(k)\bigwedge_{12}^{m}(k)}\,, \qquad \text{(A-27)}$$

where

$$\Gamma_m = \bigwedge_{22}^{m}(k)\left[\Omega^2 - \alpha^2 - \left(\frac{1-\nu}{2}\right)\left(\frac{m\pi}{\phi_e}\right)^2\right] + \bigwedge_{12}^{m}(k)\left(\frac{1+\nu}{2\nu}\right)\left(\frac{m\pi}{\phi_e}\right), \qquad \text{(A-28)}$$

and solving equations (A-20) and (A-25) for $A_m'(k)$

$$A_m'(k) = \frac{\dfrac{i\omega F}{\phi_e}\,K\delta(k-k_d)\,\cos\left(\dfrac{2m+1}{2}\,\pi\,\dfrac{\phi}{\phi_e}\right)\dfrac{\sin\left(\dfrac{2m+1}{2}\,\dfrac{\pi\delta}{\phi_e}\right)}{\left(\dfrac{2m+1}{2}\,\pi\,\dfrac{\delta}{\phi_e}\right)}\,\Gamma_m'}{\bigwedge_{11}^{m'}(k)\bigwedge_{22}^{m'}(k) - \bigwedge_{21}^{m'}(k)\bigwedge_{12}^{m'}(k)} \qquad \text{(A-29)}$$

where

$$\Gamma_m' = \bigwedge_{22}^{m'}(k)\left[\Omega^2 - \alpha^2 - \left(\frac{1-\nu}{2}\right)\left(\frac{2m+1}{2\phi_e}\,\pi\right)^2 + \bigwedge_{12}^{m'}(k)\left(\frac{1+\nu}{2\nu}\right)\left(\frac{2m+1}{2\phi_e}\,\pi\right)\right. \qquad \text{(A-30)}$$

Using equations (A-27) and (A-29) in the first of equations (A-16), and taking the inverse Fourier transform

$$w(\phi, \phi_d) = \frac{i\omega FK}{\phi_e} \sum_n \left[\left[\frac{\Gamma_m \sin\left(\frac{m\pi\phi_d}{\phi_e}\right) \frac{\sin\left(\frac{m\pi\delta}{\phi_e}\right)}{\left(\frac{m\pi}{\phi_e}\right)} \sin\left(\frac{m\pi\phi}{\phi_e}\right)}{\Lambda_{11}^{m}(k)\Lambda_{22}^{m}(k) - \Lambda_{21}^{m}(k)\Lambda_{12}^{m}(k)} \right. \right. \tag{A-31}$$

$$\left. \left. + \frac{\Gamma_m' \cos\left(\frac{2m+1}{2}\pi\frac{\phi}{\phi_e}\right) \frac{\sin\left(\frac{2m+1}{2}\pi\frac{\delta}{\phi_e}\right)}{\left(\frac{2m+1}{2}\pi\frac{\delta}{\phi_e}\right)} \cos\left(\frac{2m+1}{2}\pi\frac{\phi}{\phi_e}\right)}{\Lambda_{11}^{m'}(k)\Lambda_{22}^{m'}(k) - \Lambda_{21}^{m'}(k)\Lambda_{12}^{m'}(k)} \right] \right] e^{ik_a x}$$

where $\alpha_d = k_d a$.

The impedance at $\phi = \phi_d$ and $x = 0$ is

$$Z = \frac{F}{w(0, \phi_d)} \tag{A-32}$$

where $w(0, \phi_d)$ is given by equation (A-31). This equation is used to generate the estimates of the wavenumber drive impedances for the flat and cylindrical plates shown in Figure 1.

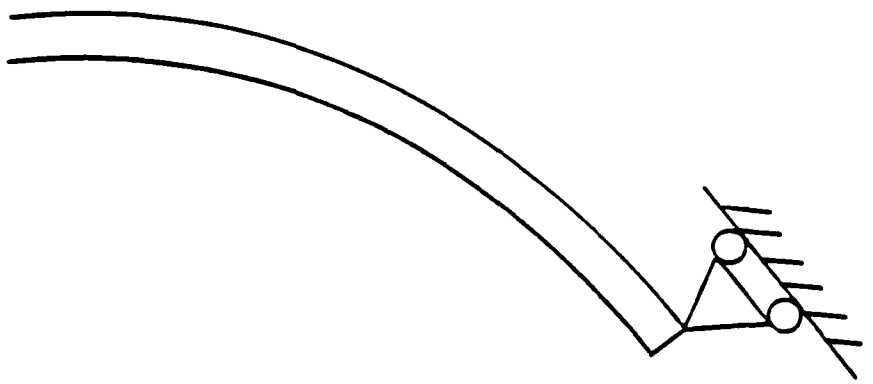

FIGURE A-1. SIMPLY-SUPPORTED BOUNDARY CONDITIONS FOR CYLINDRICAL PLATE MODEL

Appendix B

PROCEDURE FOR FLOW VISUALIZATION WITH SMOKE WIRES IN THE MODEL OF THE TRANSITION SECTION

Plywood sheets were attached to each end of the sheet metal model of the transition section. On the entrance to the model, the 2 foot by 2 foot plywood sheet was used to bolt the model to the nozzle of the open jet facility. Wax was used to smooth the surface of the junction between the model and open jet nozzle. On model exit, a 4 foot by 4 foot plywood sheet was attached to baffle secondary flow patterns at the exit. This sheet was painted flat black to reduce reflections of light from the strobe used during photography of flow patterns.

The smoke-wire technique was used to visualize the flow in the model, 4 inches upstream from the exit. As illustrated in Figure B-1, the wire was fed through a needle which penetrated the sheet metal through a 1/8-inch hole and attached to a weight which held the wire tight. Mineral oil in the plastic tube over the needle was forced through the needle opening onto the wire by air pressure generated with a small hand pump. A drop formed at the head of the needle at the top of the wire. As the drop descended down the wire, it coated the wire. Surface-tension instability caused the oil to break up into tiny droplets along the entire length of the wire. A current passed through the wire burned the oil droplets off of the wire to form a series of smoke streaks that followed the flow.

An Electro Model PS-1000-55 DC power supply provided the current to the wire. The smoke streaks were photographed with the camera aperture held open manually and the light provided by a General Radio Model 1540 Stroboscope. The camera and strobe locations are shown in Figure B-2. The photographs were taken with Kodak Tri-X 400 ASA black and white film. The timing for the current and strobe was provided by a synchronization circuit. The current was on for 0.28 seconds and the strobe triggered 0.27 seconds after the current was turned on.

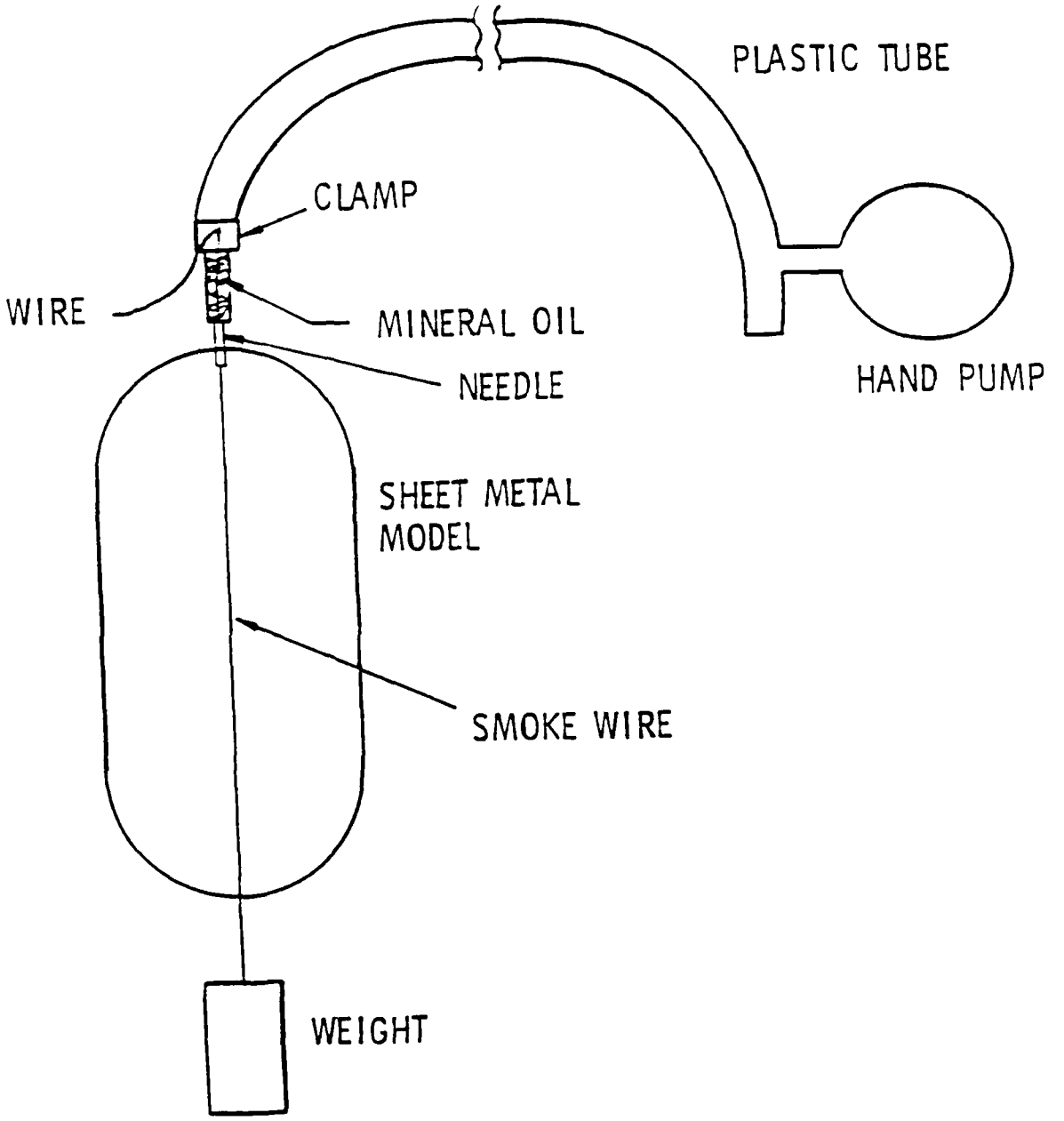

FIGURE B-1. INSTALLATION OF SMOKE WIRE IN TRANSITION SECTION MODEL

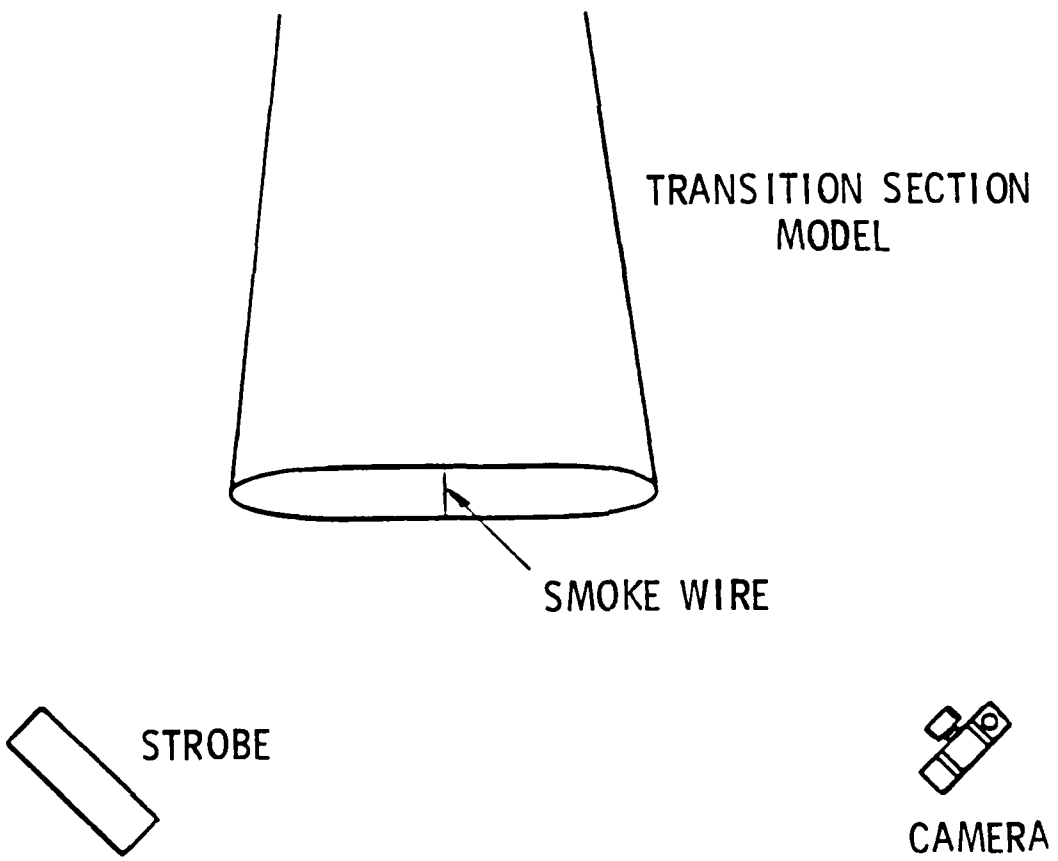

FIGURE B-2. LOCATIONS OF CAMERA AND STROBE LIGHT FOR SMOKE WIRE FLOW VISUALIZATION MEASUREMENTS IN TRANSITION SECTION MODEL

Appendix C

MATHEMATICAL ALGORITHMS FOR MAPPING TRANSITION AND DIFFUSER CROSS-SECTIONAL CONTOURS

The radius, R, and angle, θ, of each point on the cross-sectional contour at each of the specified locations along the length of the transition and diffuser sections is defined by

$$R = (1-p)R_1 + pR_2 \tag{C-1}$$

$$\theta = (1-p)\theta_1 + p\theta_2. \tag{C-2}$$

In equation (C-1), the parameter, p, is given by

$$p = 6x^5 - 15x^4 + 10x^3 \tag{C-3}$$

where x is the distance along the section normalized by the total length of 3 feet. Thus, x varies from zero to one along the length of the section. With equation (C-3), the first and second derivatives of equations (C-1) and (C-2) are zero, assuring a smooth interface of the junctions of the section to the circular cross-section of the BLRF and to the new test section, both of which remain constant along their length. In equation (C-1), R_1 is the radius of the BLRF circular cross section and R_2 is the distance from the center of the cross section to the point on the contour of the test section (See Figure C-1). Thus, for each point on the contour (e.g. the ith point in Figure C-1) equation (C-1) provides a continuous transfer from the radius at the end attached to the new test section to the other end attached to the BLRF. In equation (C-2),

$$\theta_1 = \frac{A_p}{A_t} \tag{C-4}$$

where A_p is the partial area below the radial line to the point on the contour (See Figure C-1) and A_t is the total area, and

$$\theta_2 = \tan^{-1}\left(\frac{y_2}{x_2}\right) \tag{C-5}$$

where x_2, y_2 define the point on the contour of the test section end of the transition or diffuser section. Thus, the angle of the points of the cross-sectional contour of a given location along the length of the section is varied so that the increase in the cross-sectional area produced by an increase in angle is constant. The objective of this constraint is to cause every fluid particle to experience area changes which are nearly identical and smooth in the streamwise direction.

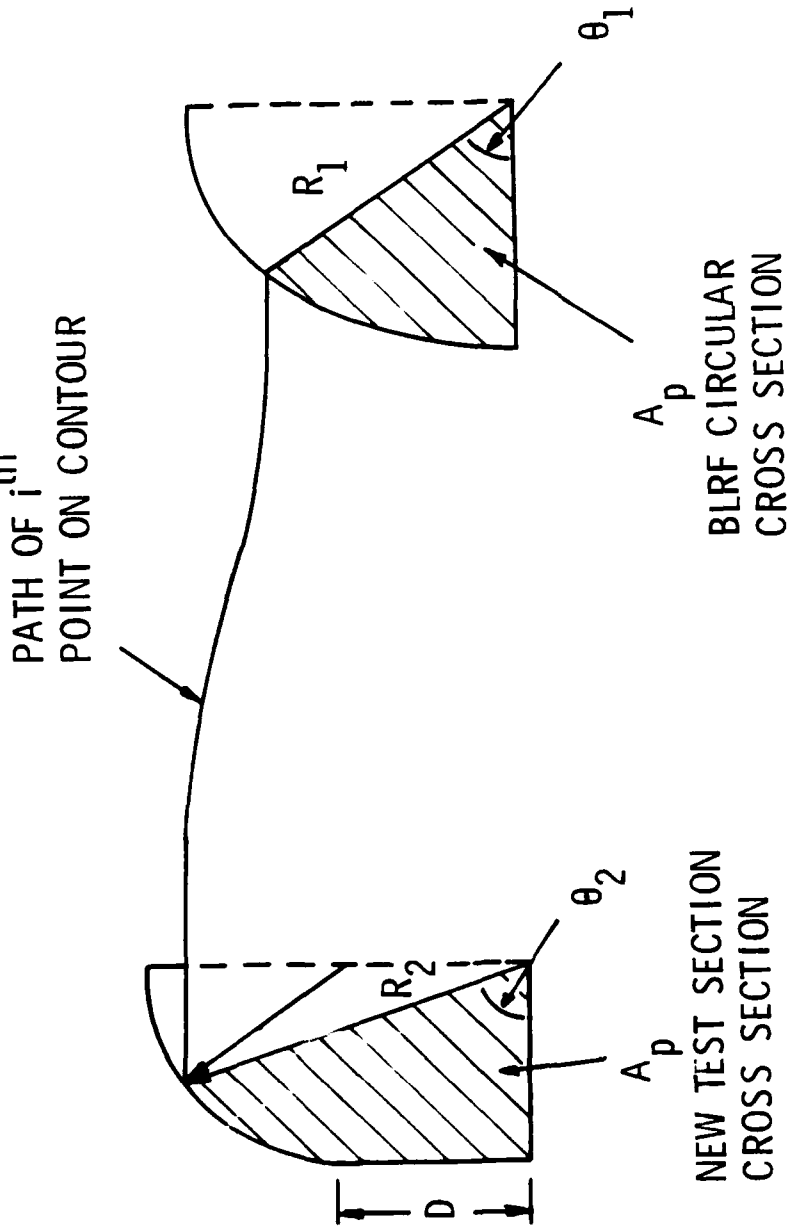

FIGURE C-1.

FIGURE C-1. METHOD OF MAPPING CONTOURS OF INNER SURFACE OF TRANSITION AND DIFFUSER SECTIONS

Appendix D

DESIGN OF CUT CONSTRAINED LAYER/PASSIVE DYNAMIC ABSORBER TREATMENT FOR THE BLRF

As discussed in Section 3.2, a cut constrained layer damping treatment is effective at low frequencies. In addition, by properly selecting the mass of the plates in the cut constraining layer and the stiffness of the damping layer, the treatment can be tuned to provide additional vibration reduction as a passive dynamic absorber at frequencies where the vibration levels are highest. The basic design of this treatment is illustrated in Figure 20.

Dynamic Absorber

The frequency to which a dynamic absorber is tuned is given by (15)

$$\omega_a^2 = \omega_o^2 \left(\frac{M_1}{M_1 + M_2} \right) \tag{D-1}$$

where ω_a is the resonant frequency of the dynamic absorber, M_1 is the mass of the untreated structure, M_2 is the mass of the dynamic absorber, and

$$\omega_o^2 = \frac{k_1}{M_1 + M_2} \tag{D-2}$$

where k_1 is the stiffness of the untreated structure. Equation (D-1) was derived for a simple oscillator with a simple oscillator dynamic absorber. At resonance, continuous structures behave like a simple oscillator so that Equation (D-1) can be applied to continuous structures, where M_1 and k_1 are the effective mass and stiffness of the structure at resonance. Since the first step in designing the dynamic absorption is to determine the tuned frequency, the effective mass and stiffness of the BLRF wall had to be determined.

At the drive point, the real part of the characteristic admittance, Y_c, is given by (9)

$$R_e(Y_c) = \frac{\pi}{2\epsilon_n M_n} \tag{D-3}$$

where ϵ_n is the frequency spacing between modes and M_n is the modal mass. Using estimates of the modal mass, the modal stiffness, k_n, was from (9)

$$k_n = \frac{1}{K_n} = \omega_n^2 M_n \tag{D-4}$$

where K_n is the modal compliance. Equations (D-3) and (D-4) were used to estimate the modal mass and stiffness from the characteristic admittance and frequency spacing of modes. The modal mass and stiffness were then used in Equations (D-1) and (D-2) to determine the tuned frequency for a selected dynamic absorber mass.

The characteristic admittance of the BLRF wall was determined from measurements. A Wilcoxen F4 shaker with an impedance head was attached to the lower leg of the BLRF at the position shown in Figure D-1. The shaker was mounted via a threaded stud to a mounting block that was epoxied to the outer surface of the BLRF wall. The shaker was excited with a pure tone frequency, swept from 20 to 1100 Hz. The force and acceleration were measured during the frequency sweep by the force gage and accelerometer in the shaker impedance head. The peak hold on the analyzer was used to reduce the data from the force gage and accelerometer. In addition to the spectra levels from the force gage and accelerometer, the phase between the force gage and accelerometer was measured. The measured phase was the phase that occurred when the level measured in each band was maximum. This occurred when the shaker drive frequency swept through the measurement band.

The real part of the characteristic admittance is given by

$$R_e(Y_c) = R_e\left(\frac{V^*}{F^*}\right) = \frac{|V^*|}{|F^*|}\cos(\phi_v - \phi_F) \qquad \text{(D-5)}$$

where F^* and V^* are the mean values of the complex force and velocity, respectively, and $(\phi_v - \phi_F)$ the difference in the phases between the velocity and force. The characteristic admittance is the admittance for the infinite structure, i.e., with the boundary effects removed. From the mean value theory (9), the admittance for an infinite structure is equal to the mean-value of the admittance of the finite structure. The measured acceleration levels are plotted in Figure D-2, along with a curve showing the mean value of acceleration. Resonances at 132, 242 and 400 Hz are evident in Figure D-2. Differences in the resonant frequencies give values of the frequency spacing, ϵ_n. The velocity is computed from the measured acceleration by dividing the acceleration by the radian frequency, ω. The measured force levels are plotted in Figure D-3 and the measured phase differences between acceleration and force is plotted in Figure D-4. The mean value of the phase in Figure D-4 is about 90°. Thus in Equation D-5, $\phi_v - \phi_F \approx 0^0$.

Using data presented in Figures D-2, D-3, D-4 in Equations D-3 and D-5 yields an effective mass of 1176×10^4 gms for the first resonance of the BLRF wall. From Equation D-4, the effective stiffness is 1.21×10^{10} dynes/cm. To begin, we assume that the constraining layer is composed of 1/8-inch thick by 1 foot long aluminum plates with the width in the direction of the circumference of the BLRF wall to be specified in tuning the damping treatment as a dynamic absorber. With the radius of the BLRF wall being 10 inches, the mass of the constraining layer is 4.17×10^3 gm. Here, we have assumed that each row of constraining layer plates around the circumference are independent of the next row. Using these values in Equation D-2 gives $\omega_o = 669$ rad/sec (106 Hz) as the frequency to which the treatment should be tuned to reduce the response of the BLRF wall at the first resonance at 132 Hz. The width of the constraining layer plates were adjusted to tune the treatment.

The first resonance of the BLRF wall measured by the single shaker at 132 Hz is probably the m = 2 circumferential bending mode where the wavelength is equal to one half the circumference. In this case, the bending wavenumber is

$$k_p = \frac{2\pi}{\lambda p} = \frac{2\pi}{\pi r} = \frac{2}{r} \qquad \text{(D-6)}$$

For the 10-inch radius, $k_p = 7.87 \times 10^{-2}$ cm^{-1}. The bending wavenumber in a plate is given by:

$$k_p^4 = \frac{12\omega^2\rho(1-\nu^2)}{h^2E} \qquad \text{(D-7)}$$

where ρ is the material density, ν is the Poisson's constant, h is the thickness and E is Young's modulus. To tune the cut constraining layer as a dynamic absorber to ω = 669 rad/sec, parameters in Equation D-7 were adjusted for ω = 669 rad/sec until the wavenumber was 7.87×10^2 cm^{-1}. With the original assumption that the thickness of the layer is 1/8-inch, the parameter to adjust is the stiffness of the constraining layer (effective Young's modulus). This is done by adjusting the shear modulus or the thickness of the damping layer.

The effective Young's modulus for the cut constraining layer results from the shearing stresses in the damping layer. In Figure D-5, a section view of the cut constraining layer and damping treatment is illustrated. A force, F, applied to the side of one of the cut constraining layer plates produces a shearing stress in the damping layer. For a shearing strain of $\Delta\theta$

$$G = \frac{F/A_s}{\Delta\theta/h_2} \qquad \text{(D-8)}$$

where G is the shear modulus of the damping layer and A_s is the contact area between the constraining plate and damping layer. The effective Young's modulus, E, for the layer is

$$E = \frac{F/A_e}{\Delta x/w} \qquad \text{(D-9)}$$

where $\Delta x = \Delta\theta h_2$ is the displacement of one of the constraining plates relative to an adjacent plate and w is the width of the constraining layer plates. The value $\Delta\theta h_2$ serves as the effective in-plane deformation of the constraining layer. Combining Equations (D-8) and (D-9)

$$E = G\,\frac{w^2}{h_2^2\,h_1} \qquad \text{(D-10)}$$

The cuts in the constraining layer minimizes Poisson's effect, so that $\nu \approx 0$.

$$k_p^4 = \frac{12\omega_2\rho h_2}{h_1 G w^2}^2 \qquad \text{(D-11)}$$

For 0.01-in. thick soundcoat Dyad 606 damping layer, which has a shear modulus of 1.7×10^8 dynes/cm^2 near the tuned frequency of 669 rad/sec., Equations D-6 and D-11 yield a width of 7/8 inches for the constraining layer plates. Therefore, a damping treatment consisting of 0.01-inch thick Dyad 606 damping layer constrained by 7/8 in. by 1 ft., 1/8-in. thick aluminum plates will act a dynamic absorber on the BLRF wall tuned to the first resonant frequency of 232 Hz.

The procedure outlined above was repeated for several damping treatments with Dyad damping layers. The results are presented in Table D-1.

Damping

The damping loss factor, η_e, for a structure with a cut constrained layer damping treatment is estimated using the following equation (14)

$$\eta_e = 12 \frac{\beta G_2}{E_1} \frac{D^2 H_{20}}{H_2 H_1^3} \left[\frac{g}{1 + g}\right] \theta \qquad \text{(D-12)}$$

where

$$\theta = 1 + \frac{g(g - 3)}{g + 1} \left[\frac{\cosh(L/D) - \cos(k_p L)}{(L/D) \sinh (L/D)}\right] + g \left[\frac{1 - \cos(k_p L) \cosh(L/D)}{\sinh^2(L/D)}\right] \qquad \text{(D-13)}$$

and

$$g = \frac{1}{k_p^2 D^2} \qquad \text{(D-14)}$$

is the shear parameter and

$$D = \frac{E_3 H_2 H_3}{G_2} \qquad \text{(D-15)}$$

In Equations D-12, D-13, D-14, and D-15, β is the damping loss factor of the damping layer, G_2 is the shear modulus of the damping layer, E_1 is the Young's modulus for the damped structure, E_3 is Young's modulus for the constraining layer, H_{30} is the distance between the centers of the constraining layer and damped structure, H_2 is the thickness of the damping layer, H_3 is the thickness of the constraining layer, k_p is the bending wavenumber of the damped structure (See Equation D-7) and L is the width of the constraining layer plates. Equation D-12 was used to predict the damping loss factors for the four treatments listed in Table D-1 on the 1/4-inch thick BLRF steel wall.

For the Soundcoat Dyad damping layer, the loss factor and shear modulus for 150^0 F, (16) are shown in Figure D-6. The predicted damping losses are presented in Figure D-7 for the four designs listed in Table D-1.

Conclusion

The masses of the 1/8 by 4 in. aluminum constraining plates are nearly equal to the masses of the 1/8 by 1 3/8 in. steel constraining plates. Therefore, as dynamic absorbers the effectiveness of these two treatments should be nearly equal. Since the masses of the constraining plates in the other two treatments are smaller, their effectiveness as dynamic absorbers will be less.

As shown in Figure D-7, damping with the 1/8 by 4 inch aluminum constraining plates on the 0.05 in. Dyad is higher than the damping with the other three treatments. Because this treatment should also be one of the most effective as a dynamic absorber, it was selected for use on the outer walls of nontest sections of the BLRF.

CONSTRAINING LAYER		THICKNESS OF DAMPING LAYER	WIDTH OF CONSTRAINING LAYER
THICKNESS	MATERIAL		
1/8 in.	Alum.	0.01 in.	7/8 in.
1/4 in.	Alum.	0.01 in.	1/2 in.
1/8 in.	Steel	0.01 in.	13/8 in.
1/8 in.	Alum.	0.05 in.	4 in.

TABLE D-1. DESIGN PARAMETERS FOR DAMPING/DYNAMIC ABSORBER TREATMENTS

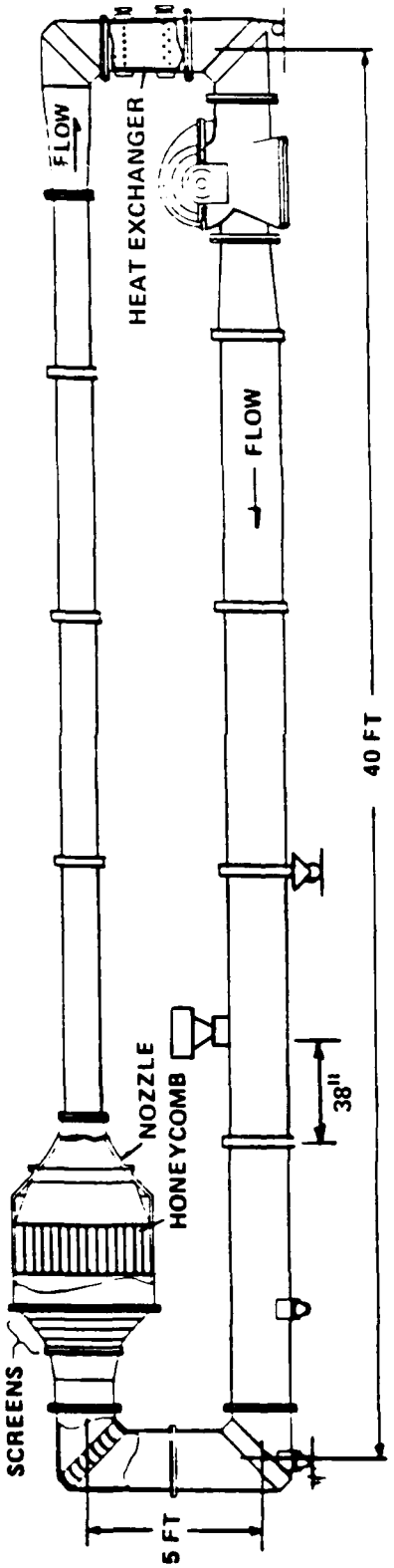

FIGURE D-1. LOCATION OF DRIVE-POINT ADMITTANCE MEASUREMENTS ON LOWER LEG OF BLRF

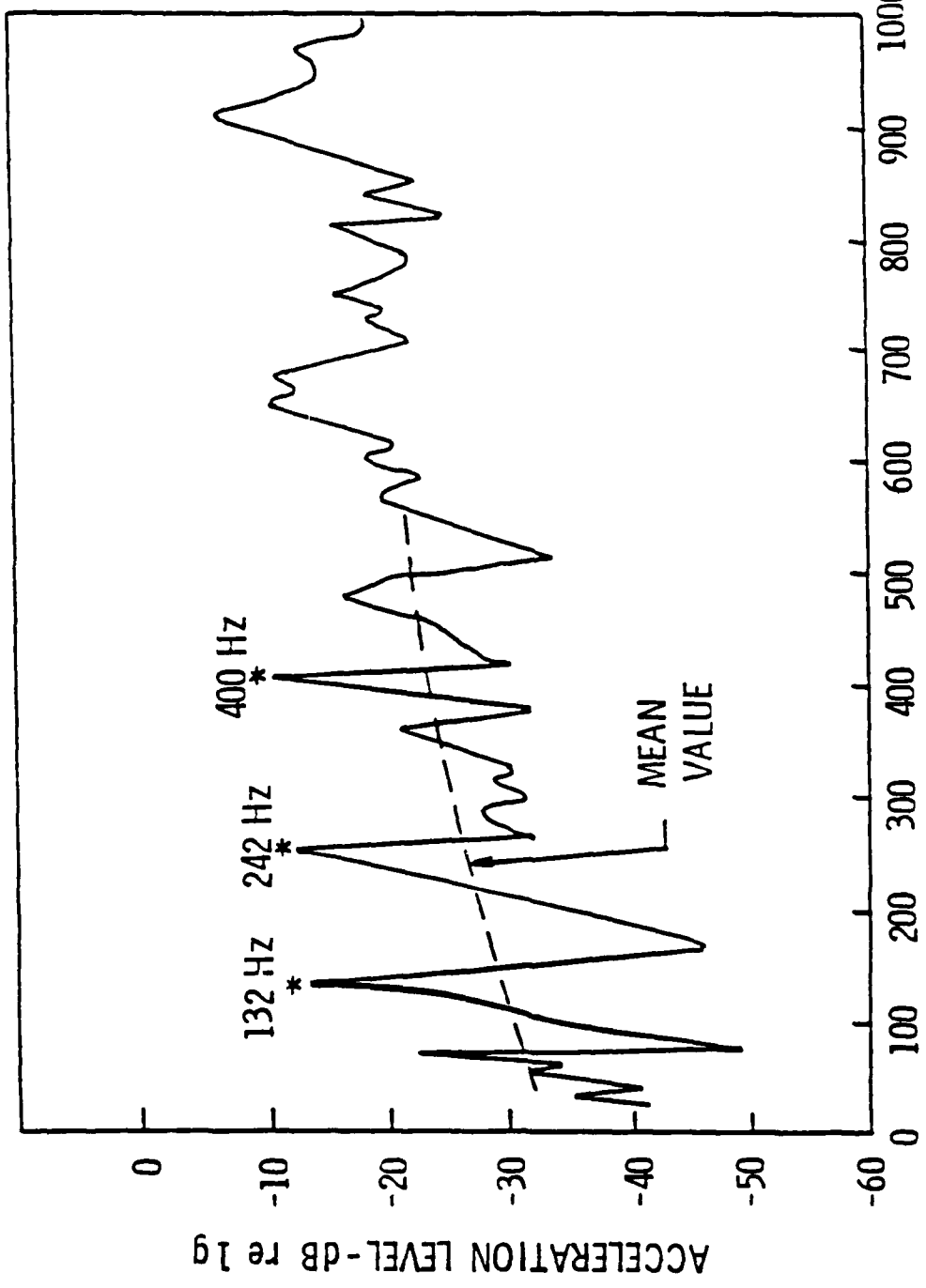

FIGURE D-2. ACCELERATION LEVELS MEASURED DURING DRIVE-POINT ADMITTANCE MEASUREMENTS ON THE BLRF

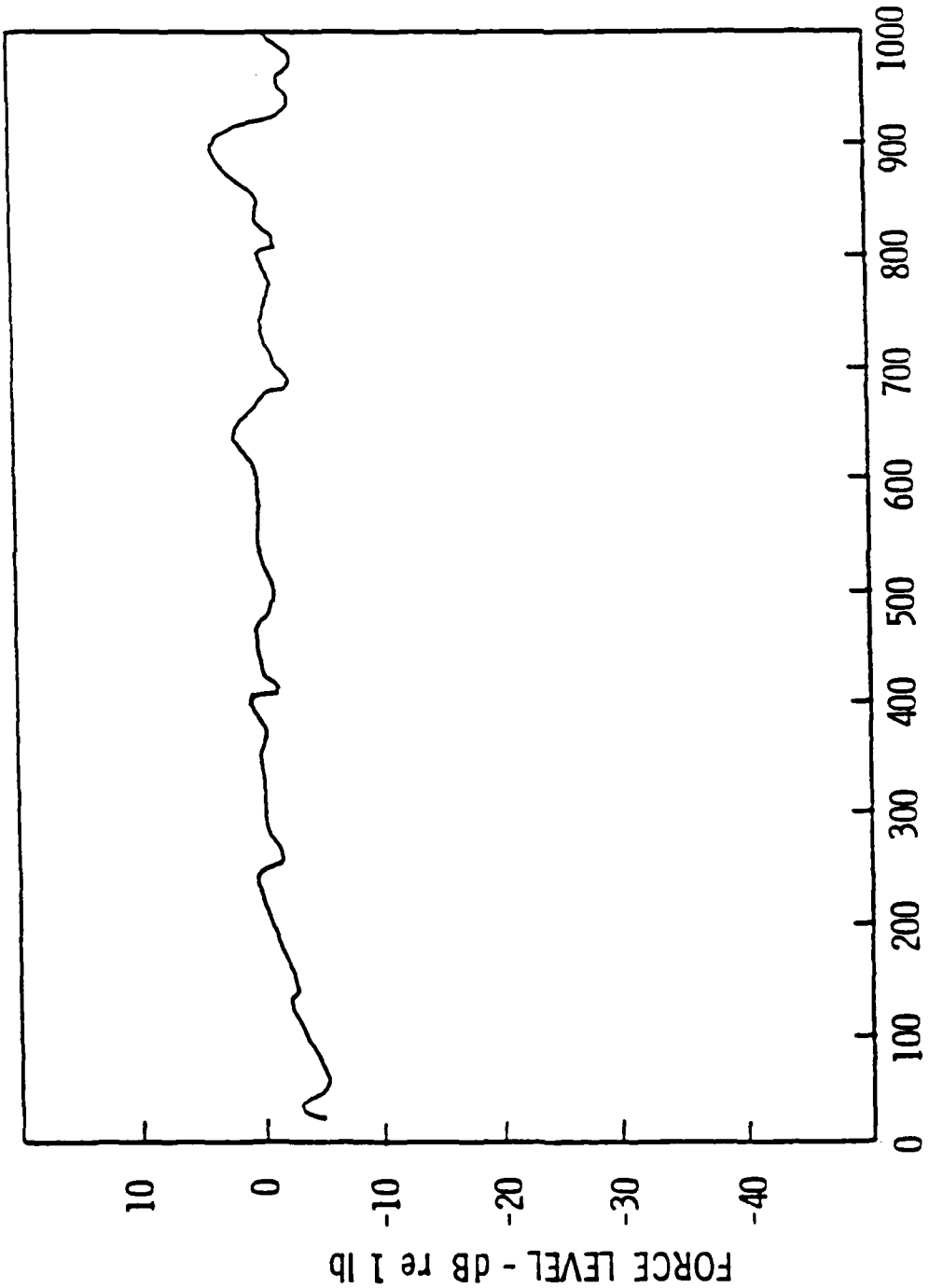

FIGURE D-3. FORCE LEVELS MEASURED DURING DRIVE-POINT ADMITTANCE MEASUREMENTS ON THE BLRF

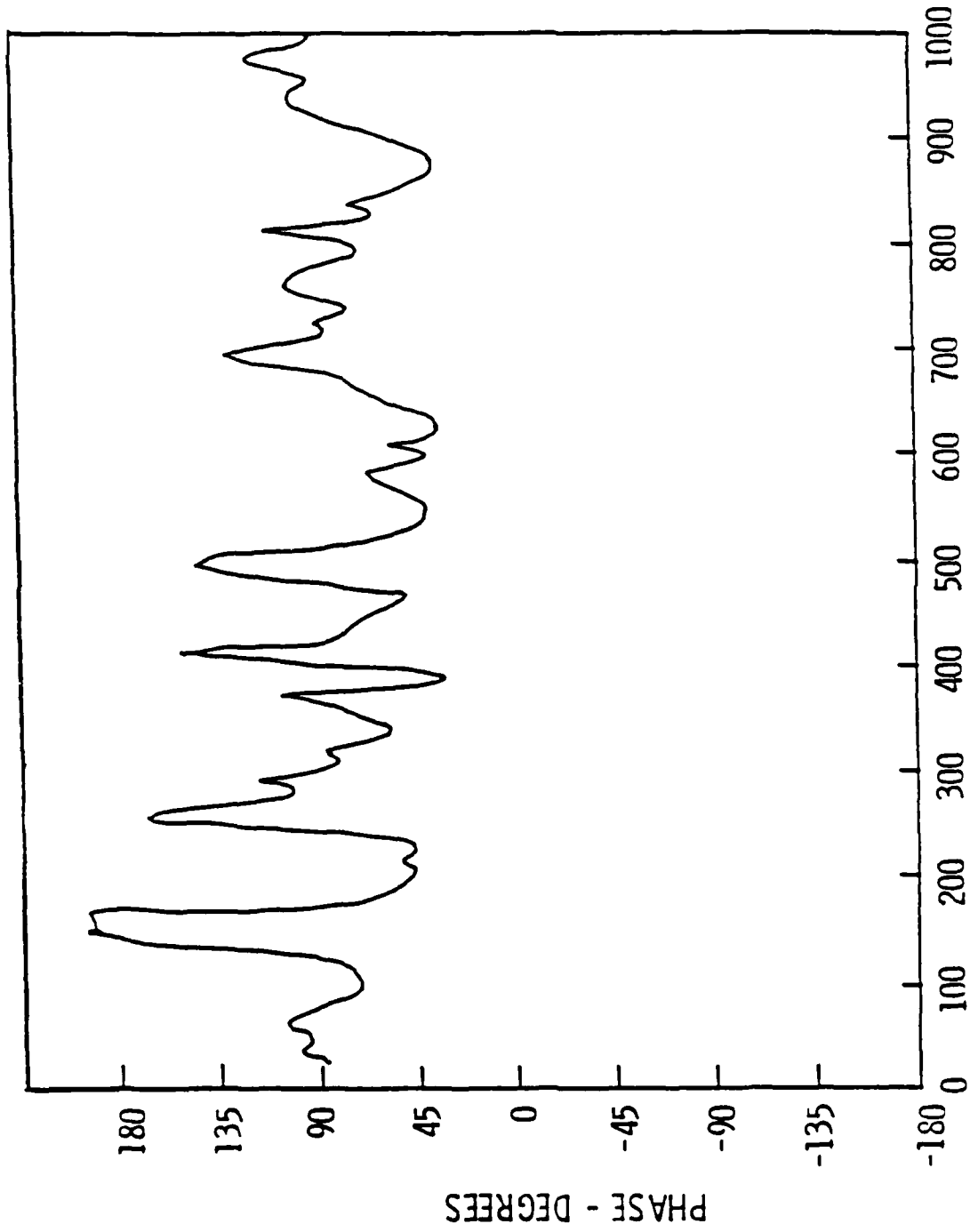

FIGURE D-4. PHASE BETWEEN FORCE AND ACCELERATION MEASURED DURING DRIVE-POINT ADMITTANCE MEASUREMENTS ON THE BLRF

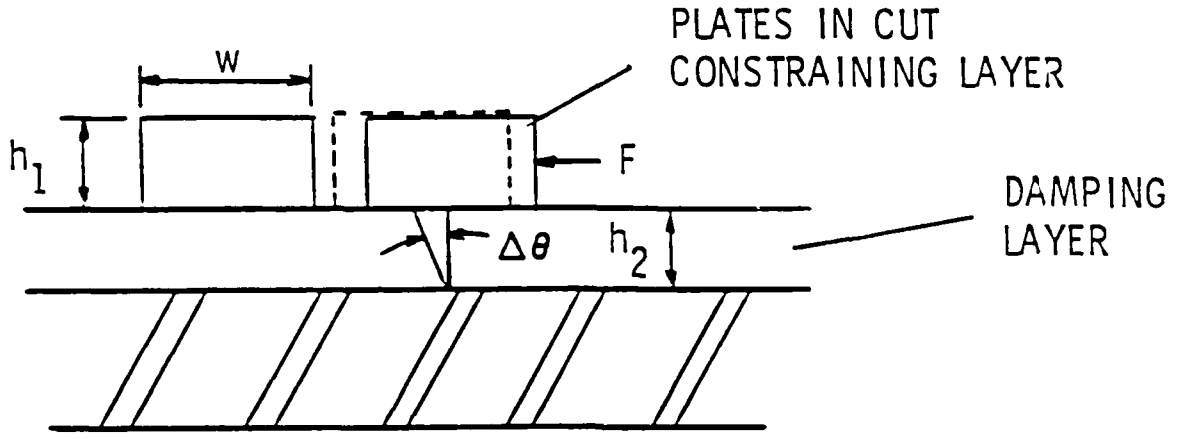

FIGURE D-5. CUT CONSTRAINED LAYER DAMPING DURING DEFORMATION

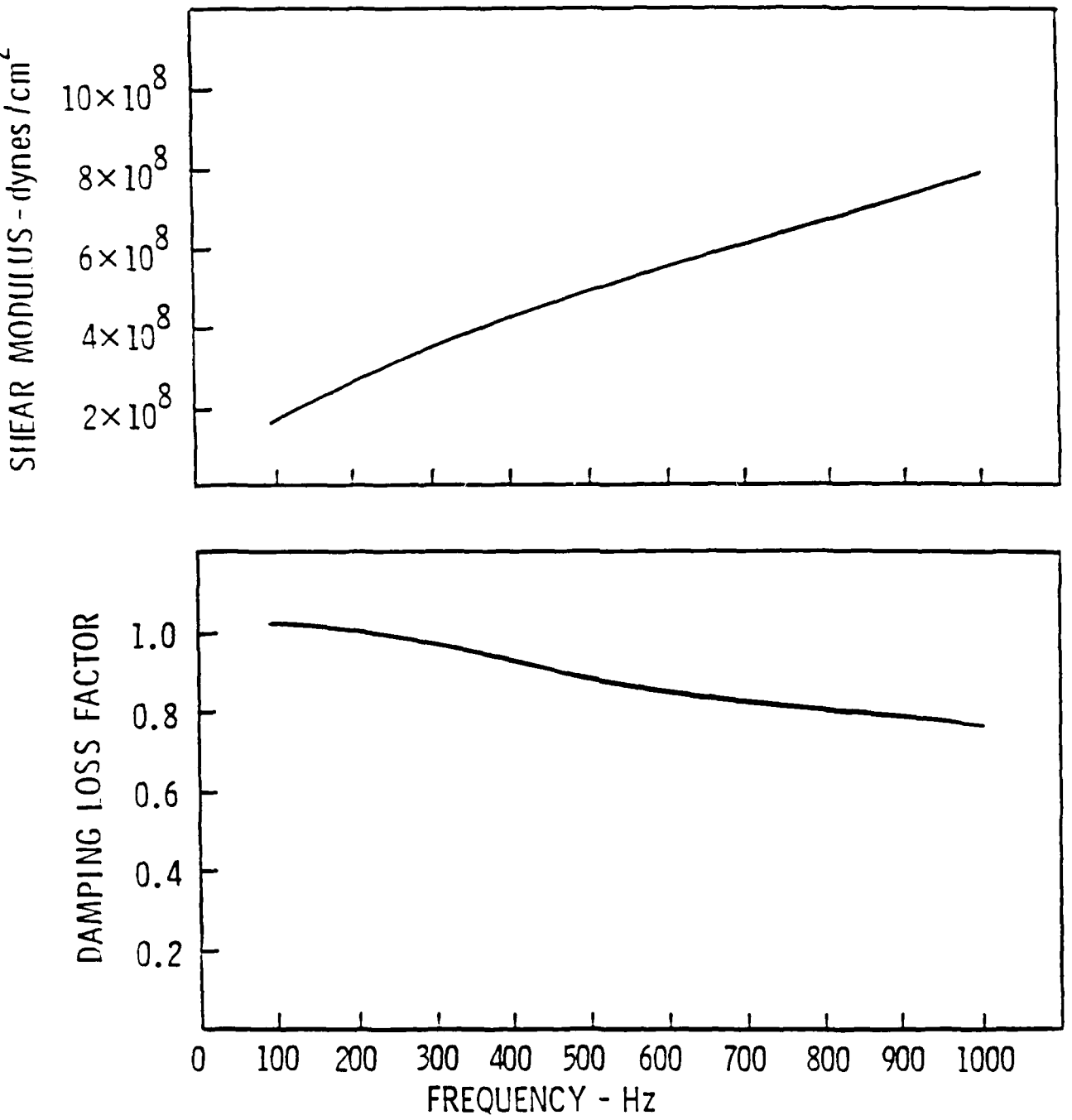

FIGURE D-6. SHEAR MODULUS AND LOSS FACTOR FOR DYAD DAMPING MATERIAL

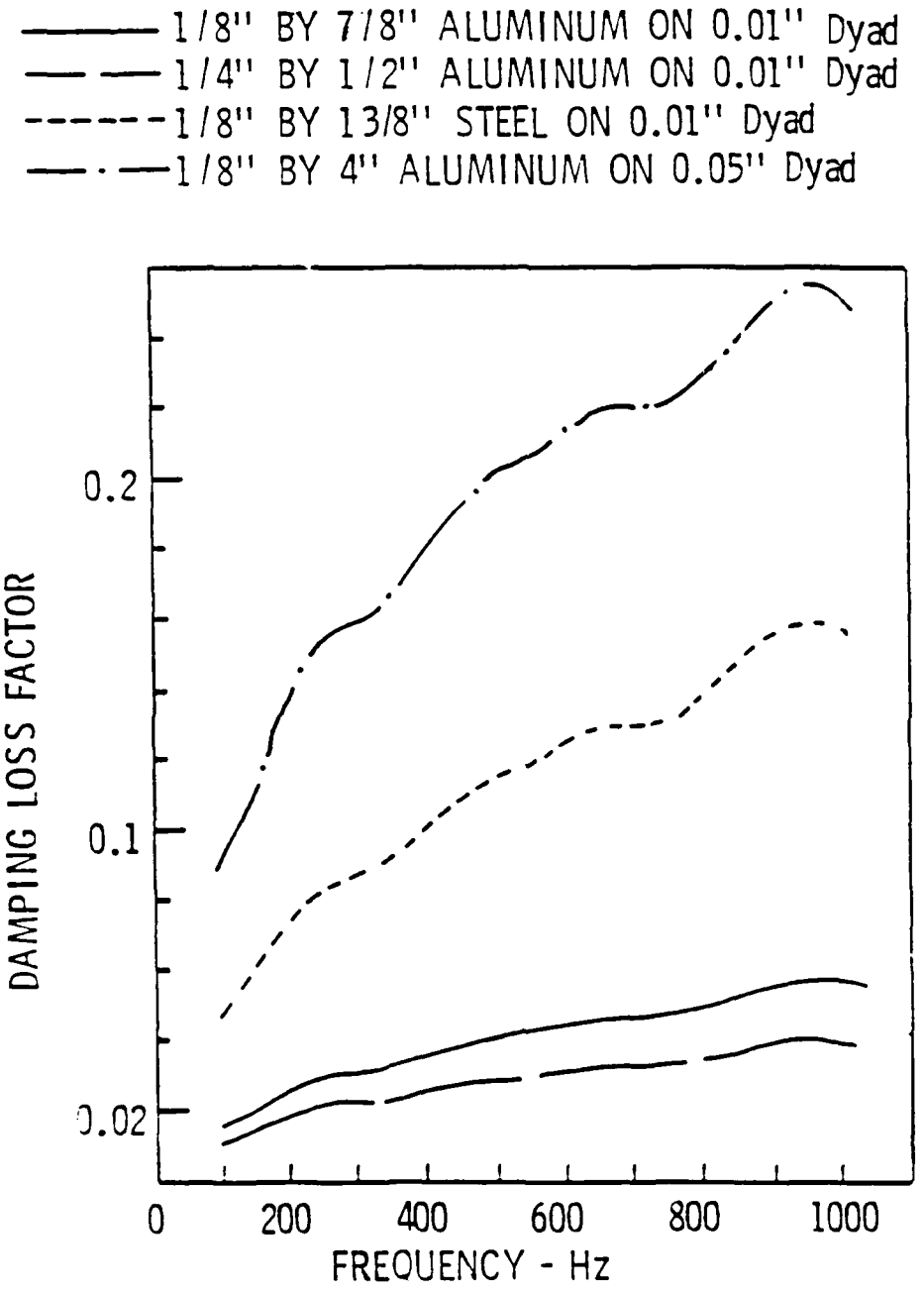

FIGURE D-7. PREDICTED DAMPING LOSS FACTORS FOR CUT CONSTRAINED LAYER TREATMENTS ON THE BLRF

DISTRIBUTION LIST FOR UNCLASSIFIED ARL TM 89-38 by C. B. Burroughs, dated 23 August 1989

Office of Naval Research
Department of the Navy
800 N. Quincy Street
Arlington, VA 22217
Attn: M. M. Reischmann
Code 430
(Copy Nos. 1, 2 & 3)

Office of Naval Research
Attn: A. J. Tucker
Code 432
(Copy No. 4)

Defense Technical Information Center
Bldg. 5, Cameron Station
Alexandria, VA 22314
(Copy Nos. 5-16)

Director
Naval Research Laboratory
Washington, DC 20375
(Copy Nos. 17-22)

David Taylor Research Center
Department of the Navy
Bethesda, MD 20084-5000
Attn: Yun-Fan Hwang
Code 1942
(Copy No. 23)

Professor P. Leehey
Dept. of Ocean Engineering
Massachusetts Institute of Technology
77 Massachusetts Avenue
Cambridge, MA 02139
(Copy No. 24)

Dr. Henry P. Bakewell
Naval Underwater Systems Center
New London
New London, CT 06320
(Copy No. 25)

Munio Cassarella
Catholic University of America
620 Michigan Avenue, N.E.
Washington, DC 20064
(Copy No. 26)

Mr. Joel Parks
Southwest Research Institute
6220 Colebrea Road
San Antonio, TX 78284
(Copy No. 27)

Mr. Norman Meese
National Institute of Standards & Technology
Gaithersburg, MD 20899
(Copy No. 28)

The Applied Research Laboratory
The Pennsylvania State University
Post Office Box 30
State College, PA 16804
Attn: C. B. Burroughs
(Copy No. 29)

Applied Research Laboratory
Attn: GTWT Files
(Copy No. 30)

Applied Research Laboratory
Attn: ARL Library
(Copy No. 31)

Applied Research Laboratory
Attn: D. E. Thompson
(Copy No. 32)

Applied Research Laboratory
Attn: S. Deutsch
(Copy No. 33)

Applied Research Laboratory
Attn: H. L. Petrie
(Copy No. 34)